NEUROSCIENCE

Regulation of blood-brain barrier integrity by *Dmp1*-expressing astrocytes through mitochondrial transfer

Delin Liu[1,2,3,4]†, Peng Liao[3,4]†, Hao Li[3,4]†, Sihan Tong[3,4], Bingqi Wang[3,4], Yafei Lu[3,4], Youshui Gao[3], Yigang Huang[3], Hao Zhou[5], Linjing Shi[5], John Papadimitriou[1,6], Yao Zong[1], Jun Yuan[1,2], Peilin Chen[1], Ziming Chen[1], Peng Ding[3,4], Yongqiang Zheng[7], Changqing Zhang[3,4]*, Minghao Zheng[1,2]*, Junjie Gao[3,4,7]*

The blood-brain barrier (BBB) acts as the crucial physical filtration structure in the central nervous system. Here, we investigate the role of a specific subset of astrocytes in the regulation of BBB integrity. We showed that *Dmp1*-expressing astrocytes transfer mitochondria to endothelial cells via their endfeet for maintaining BBB integrity. Deletion of the Mitofusin 2 (*Mfn2*) gene in *Dmp1*-expressing astrocytes inhibited the mitochondrial transfer and caused BBB leakage. In addition, the decrease of MFN2 in astrocytes contributes to the age-associated reduction of mitochondrial transfer efficiency and thus compromises the integrity of BBB. Together, we describe a mechanism in which astrocytes regulate BBB integrity through mitochondrial transfer. Our findings provide innnovative insights into the cellular framework that underpins the progressive breakdown of BBB associated with aging and disease.

INTRODUCTION

The blood-brain barrier (BBB) has a unique property of the microvasculature containing a supremely restrictive structure of cerebrovascular endothelial cells (CECs) and associated cells. The BBB protects the neural parenchyma from circulating toxins, pathogens, inflammatory lesions, traumatic injury, and various other diseases (*1*). The BBB mediates central nervous system (CNS) homeostasis by supplying essential nutrients for the brain, as well as enhancing the discharge of waste products, and regulating ionic traffic in the neural microenvironment (*2*–*4*). The function of the BBB relies on complex barrier structures, including tight junctions between CECs, surrounding mural cells, astrocytes, basal membrane, immune cells, and neural cells (*1*, *5*). Dysfunction of the BBB has emerged as a major pathological contributor in many CNS-related disorders, including brain injury, stroke, aging, and degenerative diseases such as Alzheimer's disease and Parkinson's disease (*6*–*9*). Currently, the BBB has been regarded as a critical determinant of cerebral disease severity and a substantial therapeutic target for aiding neuronal recovery (*10*, *11*). Thus, understanding the molecular mechanisms of the BBB structural and functional integrity is vital for the treatment of CNS-related disorders.

Within the CNS, astrocytes that tile the entire brain are highly heterogeneous in appearance, function, and molecular properties, and they can serve different roles and adopt distinct gene expression traits that are specific to their regional location and association with other cell types within the CNS (*12*–*14*). One of the functions of astrocytes is to act as the key mediator of CNS homeostasis by extending cellular projections that ensheath either neuronal axons or blood vessels (*15*). By covering capillaries with their endfeet, astrocytes mediate the generation and maintenance of the BBB (*5*, *16*). Astrocytes up-regulate endothelial tight junctions, polarize the expression of transporters, and influence the production of specialized enzyme systems (*5*, *17*). A recent study showed that under physiological conditions, mitochondria are enriched at the astrocyte endfeet adjacent to blood vessels (*18*) and that the enrichment of endoplasmic reticulum (ER)–mitochondria contacts in perivascular endfeet of reactive astrocytes was important for the repair of vascular injuries (*18*). However, it remains unclear as to how mitochondria within the endfeet of astrocytes are relevant to the functional integrity of the BBB in CNS homeostasis and aging. Here, we performed a series of experiments with genetically modified mice and found a population of astrocytes expressing *Dmp1* that ensheath blood vessels and transfer mitochondria to CECs to maintain the integrity of the BBB.

RESULTS

Astrocytes transfer mitochondria and alleviate oxidative stress of endothelial cells

It has been reported that mitochondria are capable of shuttling between cells by intercellular transfer, to restore tissue function in the context of physical damage or physiological imbalance (*19*–*21*). Furthermore, CECs are rich in mitochondria compared to peripheral endothelial cells (*22*), and mitochondrial stress in CECs leads to increased BBB permeability (*23*, *24*). Given the close association between astrocytes and endothelial cells, we hypothesized that

[1]Centre for Orthopaedic Research, Medical School, The University of Western Australia, Nedlands, Western Australia 6009, Australia. [2]Perron Institute for Neurological and Translational Science, Nedlands, Western Australia 6009, Australia. [3]Department of Orthopaedics, Shanghai Sixth People's Hospital Affiliated to Shanghai Jiao Tong University School of Medicine, Shanghai 200233, China. [4]Institute of Microsurgery on Extremities, Shanghai Sixth People's Hospital Affiliated to Shanghai Jiao Tong University School of Medicine, Shanghai 200233, China. [5]Department of Orthopaedics, The Second Affiliated Hospital of Zhejiang University School of Medicine, Hangzhou, Zhejiang Province 310009, China. [6]Department of Pathology, Pathwest, Nedlands, Western Australia 6009, Australia. [7]Department of Orthopaedics, Jinjiang Municipal Hospital, Jinjiang, Fujian Province, 362200, China.
*Corresponding author. Email: colingjj@163.com (J.G.); minghao.zheng@uwa.edu.au (M.Z.); zhangcq@sjtu.edu.cn (C.Z.)
†These authors contributed equally to this work.

astrocytic contact may be relevant to the mitochondrial load of CECs. To address this, we used the *CAG*^{cre}-*Cox8*^{Dendra2} mouse strain to visualize mitochondria in primary astrocytes genetically labeled with Dendra2 fluorescence (astrocytes$^{Mito\text{-}Dendra2}$) signal (fig. S1A). We then incubated primary astrocytes$^{Mito\text{-}Dendra2}$ with the CEC line bEnd.3 in a two-dimensional (2D) in vitro coculture model to observe their potential interaction. As shown, we found that Dendra2-labeled mitochondria translocated from Aquaporin-4 (AQP4)–marked astrocytes to CD31-marked bEnd.3 cells after 24 hours of coculture (Fig. 1, A and B). Real-time live imaging of the 2D coculture system also revealed the dynamic movement of mitochondria from astrocytes$^{Mito\text{-}Dendra2}$ to MitoTracker Red (MTR)-stained bEnd.3 cells (Fig. 1C). In addition, we also conducted transmission electron microscopy (TEM) imaging on 1-month-old (1M) mouse brain to demonstrate the transfer of mitochondria from astrocytes to endothelial cells in vivo. The representative TEM images indicated the close association of astrocyte mitochondria within the endfeet with endothelial cells (Fig. 1D). It appears that in the region where mitochondria are closely situated next to the endothelial cell, a portion of astrocyte plasma membrane (black arrow) was fused to the endothelial cell (Fig. 1D), facilitating the transfer of astrocyte mitochondria to endothelial cell.

Because the endfeet of astrocytes are structures that mediate CEC interactions (*25*–*27*), we then asked whether the mitochondrial transfer is mediated by these structures. Using a 3D culture system, we plated astrocytes$^{Mito\text{-}Dendra2}$ on the upper surface of Transwell membranes to promote the extension of their distal dendrites (Fig. 1E). As shown by the lateral view of Z-series confocal imaging on the Transwell membrane, we found that astrocytes extend distal processes, which are similar to endfeet structure in vivo and are rich in mitochondria, to the undersurface of the Transwell membrane (Fig. 1F). Next, we cocultured astrocytes$^{Mito\text{-}Dendra2}$ in the upper chamber of Transwell and bEnd.3 endothelial cells on the bottom coverslip of inserted culture wells to mimic the cellular assembly process between these cell types to form a BBB network (Fig. 1G) (*28*). After 24 hours of coculturing, we found Dendra2-fluorescent mitochondria within the soma and distal end of AQP4-labeled astrocytes$^{Mito\text{-}Dendra2}$ processes, as shown by the different Z-stacks of the confocal imaging on Transwell membranes (Fig. 1H). In the meantime, confocal imaging also showed that bEnd.3 cells (labeled by CD31) on the coverslip acquired mitochondria from astrocytes$^{Mito\text{-}Dendra2}$ after coculturing (Fig. 1I), indicating intercellular mitochondrial transfer from astrocytes to endothelial cells.

It has been shown that oxidative stress, detected within endothelial cells as an accumulation of reactive oxygen species (ROS), contributes to BBB leakage (*29*–*31*). To verify whether mitochondria transferred from astrocytes to endothelial cells modulate ROS accumulation, we conducted 3D cocultures of astrocytes$^{Mito\text{-}Dendra2}$ and damaged or healthy bEnd.3 cells that were pretreated with or without mitochondrial complex inhibitors antimycin A and rotenone (A/R), respectively. Flow cytometry analysis revealed that, following the 24 hours of normal culture before cell analysis, mitochondrial ROS (MitoSOX) levels were significantly elevated after 3 hours of A/R treatment in a dose-dependent fashion (fig. S1B). After coculturing in the 3D system for 24 hours, followed by flow cytometry, we found that astrocytes transferred more mitochondria to 2/2 μM A/R-damaged bEnd.3 cells compared to healthy bEnd.3 cells (Fig. 1J). To validate whether A/R treatment causes leakage of the plasma membrane in bEnd.3 cells and thus encourages mitochondria to leak into the unhealthy, damaged bEnd.3 cells, we further evaluated the permeability of endothelial plasma membrane by conducting a Trypan Blue assay with a positive control of 0.1% Triton X-100 treatment for 5 min, and the results showed that A/R treatment did not cause significant plasma membrane leakage of endothelial cells (fig. S1C). Several studies have shown that increased ROS stress in damaged mitochondrial recipient cells can trigger mitochondrial delivery (*32*, *33*). To investigate whether ROS elevation in A/R-treated endothelial cells promotes the mitochondrial uptake in endothelial cells, we used the ROS scavenger *N*-acetyl-L-cysteine (NAC) on 2/2 μM A/R-damaged bEnd.3 endothelial cells. The result indicated that NAC is capable of scavenging the ROS accumulation in damaged bEnd.3 cells in a dose-dependent manner during 24 hours of coculture (fig. S1D). Next, we treated the A/R-damaged endothelial cells with NAC at doses of 1 and 3 mM for 24 hours before their coculture with astrcoyets^{Dendra2}. Our results of flow cytometry analysis showed that NAC significantly reduced the elevated mitochondrial transfer efficiency after A/R treatment on endothelial cells (fig. S1E). The results indicate that the increased oxidative ROS stress of endothelial cells triggers more mitochondrial transfer from astrocytes.

Last, we asked whether the mitochondrial crisis in endothelial cells induced by A/R treatment could be alleviated by extrinsic mitochondrial transfer from astrocytes. To address this, we pre-exposed bEnd.3 endothelial cells with 2/2 μM A/R before coculturing them with astrocytes$^{Mito\text{-}Dendra2}$. We found that the levels of MitoSOX signal in A/R-treated "damaged" endothelial cells were significantly elevated compared with healthy counterparts, while coculturing of A/R-treated endothelial cells with astrocytes$^{Mito\text{-}Dendra2}$ resulted in a significant reduction of MitoSOX levels (Fig. 1K). Together, these results demonstrate that astrocytes can transfer their mitochondria into endothelial cells to alleviate their mitochondria-mediated oxidative stress following exposure to A/R.

Astrocytes express *Dmp1* specifically adhere onto blood vessels

It is well recognized that astrocytes are heterogeneous in composition across the CNS and feature region-specific gene expression signatures that are correlated with their site-specific functions (*14*, *15*, *34*). Because of this, we reasoned that astrocytes that have the ability of transferring mitochondria to endothelial cells may have distinct gene expression traits that are related to their association with CECs. To address this, we performed high-throughput single-cell RNA sequencing (scRNA-seq) of mouse brains obtained from 1M, 6-month-old (6M), and 20-month-old (20M) wild-type (WT) mice and looked for potential gene expression signatures. After quality filtering (see Materials and Methods), a total of 19,847 cells were analyzed [4557 cells from 1M mice, 6270 cells from 6M mice, and 9020 cells from 20M mice (fig. S2, A and B)] and clustered into known lineages demarcated by their expression of multiple marker genes for microglia, astrocytes, smooth muscle cell (SMCs), endothelial cells, oligodendrocytes, oligodendrocyte precursor cells (OPC), pericytes, choroid plexus epithelial cells (CPCs), γ-aminobutyric acid–releasing (GABAergic) neurons, glutamatergic neurons, ependymal cells, fibroblasts, neutrophils, macrophages, T cells, and B cells (fig. S2, C nd D). As there was no age impact on the identification of cell populations, we then pooled all of the identified 4531 astrocytes from three different ages to categorize the subtypes of astrocytes. By recluster analysis of astrocytes, we found that there were 10 distinct

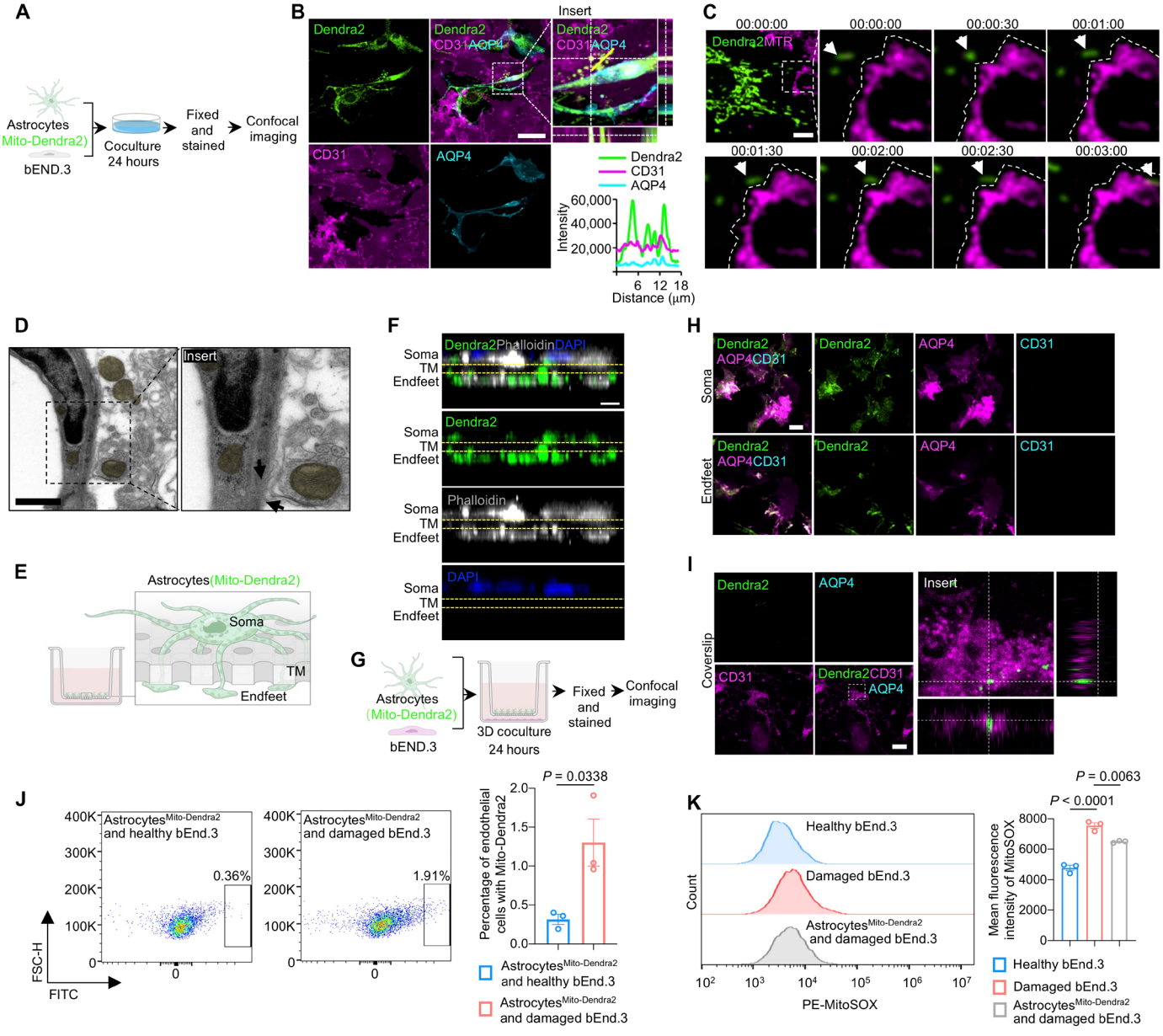

Fig. 1. Astrocytes transfer mitochondria and alleviate oxidative stress of endothelial cells. (**A**) Flowchart of 2D coculture of primary astrocytes$^{Mito\text{-}Dendra2}$ and bEnd.3 endothelial cells. (**B**) Representative confocal images and intensity wave showing Dendra2-labeled mitochondria translocated from primary astrocytes$^{Mito\text{-}Dendra2}$ (AQP4) to endothelial cells (CD31) in 2D coculture system. Scale bar, 50 μm. (**C**) Time lapse confocal images show astrocytes$^{Mito\text{-}Dendra2}$ mitochondria (Dendra2) moving dynamically toward the adjacent MitoTracker Red-labeled endothelial cell. Scale bar, 10 μm. (**D**) Representative TEM image shows the perivascular mitochondria (yellow) of astrocytes outside the endothelial plasma membrane and the mitochondria (yellow) within capillary. Scale bar, 10 μm. (**E**) Schematic of primary astrocytes$^{Mito\text{-}Dendra2}$ extending distal dendrites through the pores of a Transwell membrane (TM) and forming endfeet-like structures on the underside of the well. (**F**) The 3D lateral confocal images of TM show the distribution of mitochondria in the soma and distal dendrites of primary astrocytes$^{Mito\text{-}Dendra2}$ plated on the TM. Scale bars, 20 μm. (**G**) Flowchart of 3D coculture of primary astrocytes$^{Mito\text{-}Dendra2}$ and bEnd.3 endothelial cells. (**H**) Confocal images of the upper side (soma) and under side (endfeet) of TM showing the enrichment of mitochondria in astrocytes soma and distal end of processes (AQP4). Scale bars, 20 μm. (**I**) Confocal images of CD31-labeled bEnd.3 on coverslip show the mitochondria transferred from primary astrocytes$^{Mito\text{-}Dendra2}$ on TM. Scale bars, 20 μm. (**J**) Representative scatter plot and quantitative results of the percentage of bEnd. Three endothelial cells containing Mito-Dendra2 fluorescence in all endothelial cells pretreated with or without 2 μM A/R after coculturing with primary astrocytes$^{Mito\text{-}Dendra2}$ ($n = 3$). Two-tailed Student's unpaired *t* test. Data are presented as means ± SEM. (**K**) Representative histogram overlays and quantitative results of MitoSOX intensity in healthy bEnd.3 cells, 2 μM A/R-damaged bEnd.3 cells, and 2 μM A/R-damaged bEnd.3 cells cocultured with primary astrocytes$^{Mito\text{-}Dendra2}$ cells ($n = 3$). One-way analysis of variance (ANOVA) followed by Tukey's post hoc test. Data are presented as means ± SEM.

subclusters (cluster 0 to cluster 9) of astrocytes according to the top-enriched marker genes in different subclusters (Fig. 2, A and B). In particular, by T-distributed stochastic neighbor embedding (tSNE) plotting, we found that there were five major "clouds" of cells (clusters 0, 1, 3, and 5; cluster 2, 4 and 8; cluster 6; cluster 7; cluster 9) (Fig. 2A). Notably, clusters 0, 1, 3, and 5 were grouped together, as well as clusters 2, 4, and 8. In both cases, grouped clusters were much more similar to each other (Fig. 2A). On the other hand, subclusters grouped at a distance from the centre of the tSNE plot, such as clusters 6, 7, and 9, indicated that these astrocytes were distinct in their RNA features (Fig. 2A).

Next, we looked at the expression levels of canonical astrocyte genes across cell clusters to identify an RNA expression signature for astrocytes that form endfeet around CECs. We began by examining the expression of *Aqp4*, a gene that encodes an essential water channel protein (AQP4) at the endfeet of astrocytes abutting cerebral microvessels, to mediate water and ion homeostasis within the CNS (*35*, *36*). We postulate that astrocytes adhering to microvessels

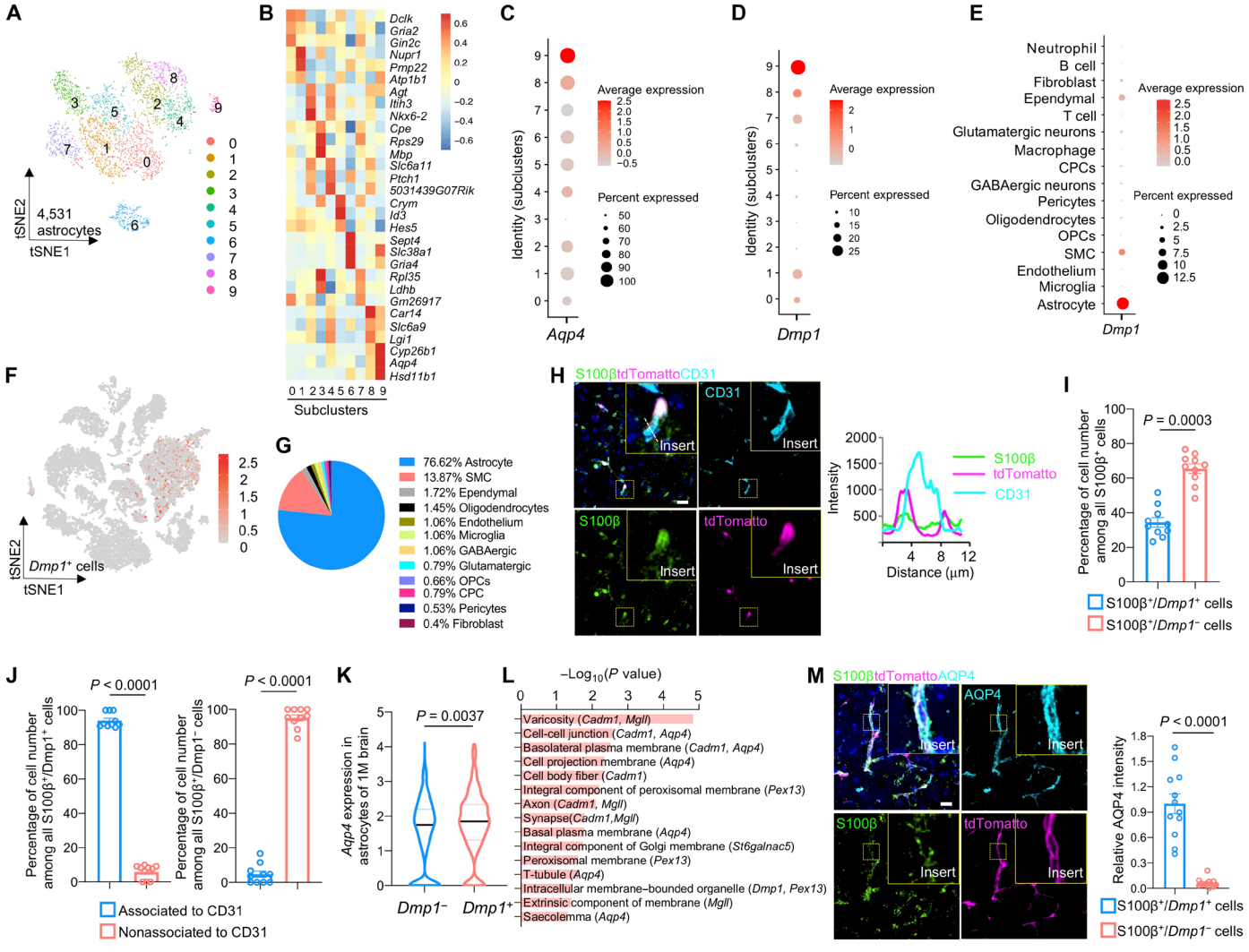

Fig. 2. A subset of astrocytes that express *Dmp1* specifically adhere to blood vessels. (**A**) tSNE plot of reclustered astrocytes ($n = 4531$ cells) reveals cellular heterogeneity of brain astrocytes. (**B**) Heatmap of the top three marker genes for subcluster identification of all astrocytes. (**C**) Bubble plot of *Aqp4* expression in different astrocytes subclusters. (**D**) Bubble plot of expression distribution for *Dmp1* in all astrocytes subclusters. (**E**) Bubble plot of *Dmp1* expression in different brain cells. (**F**) Feature plots of expression distribution for *Dmp1* in all captured single-cell events of scRNA-seq. Expression levels are color-coded as in tSNE plot. (**G**) Pie diagram of the cell types proportion among all *Dmp1*$^+$ cells from the pool of 1M, 6M, and 20M mouse brains. (**H**) Representative confocal images and fluorescence intensity analysis of CD31-labeled endothelial cells, S100β-labeled astrocytes and tdTomato-marked *Dmp1*$^+$ cells in sagittal brain sections of 1M *Dmp1*^{Cre}-*Ai9* male mice thalamus. Scale bar, 20 μm. (**I**) Quantitative analysis of the percentage of S100β$^+$/*Dmp1*$^+$ cell number or S100β$^+$/*Dmp1*$^-$ cell number among all S100β$^+$ cells ($n = 10$ images from three mice). Two-tailed Student's paired *t* test. Data are presented as means ± SEM. (**J**) Quantitative analysis of the percentage of cell number that are associated or nonassociated with CD31-labeled endothelial cells among all S100β$^+$/*Dmp1*$^+$ cells (left) or S100β$^+$/*Dmp1*$^-$ cells (right) ($n = 10$ images from three mice per group). Two-tailed Student's paired *t* test. Data are presented as means ± SEM. (**K**) Gene expression level of *Aqp4* in *Dmp1*$^+$ and *Dmp1*$^-$ astrocytes at 1M. Wilcoxon rank sum test. Data are presented as median. (**L**) Significantly up-regulated GO cellular component terms in *Dmp1*$^+$ astrocytes compared to *Dmp1*$^-$ astrocytes at 1M. (**M**) Representative confocal images and quantitation of AQP4 expression among S100β$^+$/*Dmp1*$^+$ astrocytes and S100β$^+$/*Dmp1*$^-$ astrocytes in sagittal brain sections of 1M *Dmp1*^{Cre}-*Ai9* male mice thalamus ($n = 12$ images from three mice). Scale bar, 20 μm. Two-tailed Student's paired *t* test. Data are presented as means ± SEM.

would likely be expressing *Aqp4* dominantly. We thus examined *Aqp4* gene expression across all astrocyte subclusters. As shown, subcluster 9 astrocytes are highly rich in expression of *Aqp4* (Fig. 2C), which also serves as the top marker gene of astrocytes in this subcluster (Fig. 2B), while varying levels of *Aqp4* are expressed across all other subclusters (Fig. 2C). After comparing the up-regulated terms of gene ontology (GO) enrichment between subcluster 9 and other subclusters, the results showed that plasma membrane and cell junction of subcluster 9 appear as the obvious terms among all the top 1 ranked up-regulated cellular component terms compared with all the other 10 subclusters of astrocytes (fig. S3A). Our analysis of enriched genes in subcluster 9 also identified that dentin matrix protein 1 (DMP1), an extracellular phosphorylated glycoprotein that belongs to the small integrin-binding ligand N-linked glycoprotein family (*37*, *38*), is highly enriched in strocytes of subcluster 9 when compared with astrocytes in other subclusters (Fig. 2D). Previous studies found that DMP1 is expressed in mouse brain astrocytes, and its glycosylation influences cell adhesion between astrocytes and vascular endothelial cells (*39*). Consistent with the previous finding, our gene expression matching analysis also showed that astrocytes are the overwhelming cell population that express *Dmp1* (astrocytes^{Dmp1}) among all of the analyzed brain cells (Fig. 2, E and F). Quantitation of all *Dmp1*$^+$ cells further revealed the major proportion of astrocytes (nearly 77%) among different cell types of *Dmp1*$^+$ cells (Fig. 2G). These results suggest that astrocytes of subcluster 9 with the high coexpression of *Dmp1* and *Aqp4* are those having a plethora of endfeet that are adhered to blood vessels.

Next, we investigated whether astrocytes that prominently express *Dmp1* and *Aqp4* adhere to CNS blood vessels. To achieve this objective, we first generated a transgenic *Dmp1*^{Cre}*-mGmT* mouse strain in which cells expressing *Dmp1* (*Dmp1*$^+$ cells) are specifically labeled by tdTomato fluorescence (fig. S4A). As shown, confocal imaging of brains from 1M *Dmp1*^{Cre}*-mGmT* mice revealed that *Dmp1*$^+$ cells were present in various areas of brain (fig. S4, B and C), but the thalamus, where blood vessels are abundant (*40*), poses the highest signal density of *Dmp1*$^+$ cells (fig. S4D). Consistent with our scRNA-seq clustering data, confocal imaging and intensity wave analysis of *Dmp1*^{Cre}*-mGmT* mice showed a high coexpression of AQP4 in *Dmp1*$^+$ cells at thalamus (fig. S5, A and B) and cortex (fig. S5, E and F). Further quantification revealed that 92.68 and 94.02% of *Dmp1*$^+$ cell signals in the thalamus (fig. S5C) and cortex (fig. S5G), respectively, are colocalized with AQP4. In addition, 91.18 and 79.61% of AQP4 signals in the thalamus (fig. S5D) and cortex (fig. S5H), respectively, are colocalized with *Dmp1*$^+$ cells. These results suggest that astrocytes^{Dmp1} are characterized by highly polarized endfeet. To investigate the relationship between astrocytes^{Dmp1} and blood vessels, we performed immunostaining with the endothelial cell marker CD31 on *Dmp1*^{Cre}*-mGmT* mice brain sections. Confocal imaging and intensity wave analysis revealed that the majority of astrocytes^{Dmp1} (tdTomato) extend their endfeet to wrap around, rather than colocalize with CD31-labeled endothelial cells at thalamus (fig. S5, I and J) and cortex (fig. S5, M and N). The fluorescence intensity of astrocytes^{Dmp1} (tdTomato) contacted with endothelial cells (within 10 μm) were correlated yet distinct across different brain regions (98.03% in the thalamus) (fig. S5K) and 86.27% in the cortex (fig. S5O). Likewise, 84.37 and 60.51% of CD31-labeled endothelial cells in the thalamus (fig. S5L) and the cortex (fig. S5P), respectively, were contacted with astrocytes^{Dmp1}.

To further clarify the specificity of this population of astrocytes, we compared the association of *Dmp1*$^+$ and *Dmp1*$^-$ astrocytes with blood vessels by using another transgenic fluorescent mouse line, *Dmp1*^{Cre}*-Ai9* (fig. S5Q). We stained a commonly expressed astrocyte marker (S100β) and endothelial marker (CD31) on brain sections of *Dmp1*^{Cre}*-Ai9* mice and compared their association with blood vessels between *Dmp1*$^+$ and *Dmp1*$^-$ astrocytes in the thalamus by quantifying the cell numbers of S100β$^+$ and *Dmp1*$^+$ cells (Fig. 2H). We showed the colocalization of *Dmp1*$^+$ cells with S100β$^+$ astrocytes and close association of *Dmp1*$^+$ cells with endothelial cells (CD31) and quantified that 34% S100β positive astrocytes express *Dmp1* (tdTomato) (Fig. 2I). By quantifying the S100β fluorescence signals that are associated to CD31 signals within 10 μm, we demonstrate that only S100β$^+$/*Dmp1*$^+$ but not S100β$^+$/*Dmp1*$^-$ astrocytes closely abut onto blood vessels (Fig. 2J). To explore why *Dmp1*$^+$ astrocytes have the feature to adhere to the vessel, we further analyzed the scRNA-seq data and showed that *Dmp1*$^+$ astrocytes express a significantly higher level of *Aqp4* compared with *Dmp1*$^-$ astrocytes (Fig. 2K). The GO enrichment analysis of up-regulated cellular components between *Dmp1*$^+$ and *Dmp1*$^-$ astrocytes indicates that compared to *Dmp1*$^-$ astrocytes, *Dmp1*$^+$ astrocytes present with a greater degree of terms related to cell-cell junctions, basolateral plasma membrane, and cell projection membrane along with their related genes (Fig. 2L). To further confirm the differences of AQP4 expression between *Dmp1*$^+$ and *Dmp1*$^-$ astrocytes, we costained AQP4 protein with the astrocyte marker, S100β, and found that S100β$^+$/*Dmp1*$^+$ astrocytes express higher levels of AQP4 as compared with the S100β$^+$/*Dmp1*$^-$ astrocytes (Fig. 2M). Together, these results indicated that *Dmp1*-expressing astrocytes present a specific characteristic of highly polarized endfeet that contact endothelial cells lying adjacent to the BBB.

Astrocytes^{Dmp1} transfer mitochondria to CECs in vivo

Next, we investigate whether mitochondrial transfer takes place in vivo between astrocytes^{Dmp1} and vascular endothelial cells. We created the *Dmp1*^{Cre}*-Cox8*^{Dendra2} mouse strain to specifically label mitochondria in *Dmp1*$^+$ cells (fig. S6A). Next, we performed scRNA-seq analysis using the brains of two *Dmp1*^{Cre}*-Cox8*^{Dendra2} male mice at 1M of age in which the cell suspensions were gated for Dendra2 by fluorescence-activated cell sorting (FACS) (Fig. 3A). After standard sequencing and quality control, cell types of all Dendra2-sorted cells were identified (fig. S6, B to D). Next, by matching *Dmp1* expression in all enriched cells, all the *Dmp1*-negative cells were reclustered and identified (Fig. 3, B and C). Considering that endothelial cells barely express *Dmp1* (Fig. 2, E and F) and astrocytes^{Dmp1} are closely associated with endothelial cells (Fig. 2, H and J), the results reveal that endothelial cells were a major cell type that acquired extrinsic mitochondria from astrocytes^{Dmp1} (Fig. 3, B and C). In addition, by conducting flow cytometry analysis on dissociated *Dmp1*^{Cre}*-Cox8*^{Dendra2} mouse brains, we investigated the proportion of endothelial cells incorporating astrocytes^{Dmp1}-originated mitochondria among all brain endothelial cells. Our data showed that an average of 13.8% of CD31-marked endothelial cells acquired astrocytes^{Dmp1}-originated mitochondria in the total mouse brain (Fig. 3D).

To visualize intercellular mitochondrial transfer from astrocytes^{Dmp1} to endothelial cells, we performed immunostaining and confocal microscopy imaging on *Dmp1*^{Cre}*-Cox8*^{Dendra2} mouse brain sections. Immunostaining of AQP4 on *Dmp1*^{Cre}*-Cox8*^{Dendra2} mouse brain sections revealed enrichment of mitochondria within the

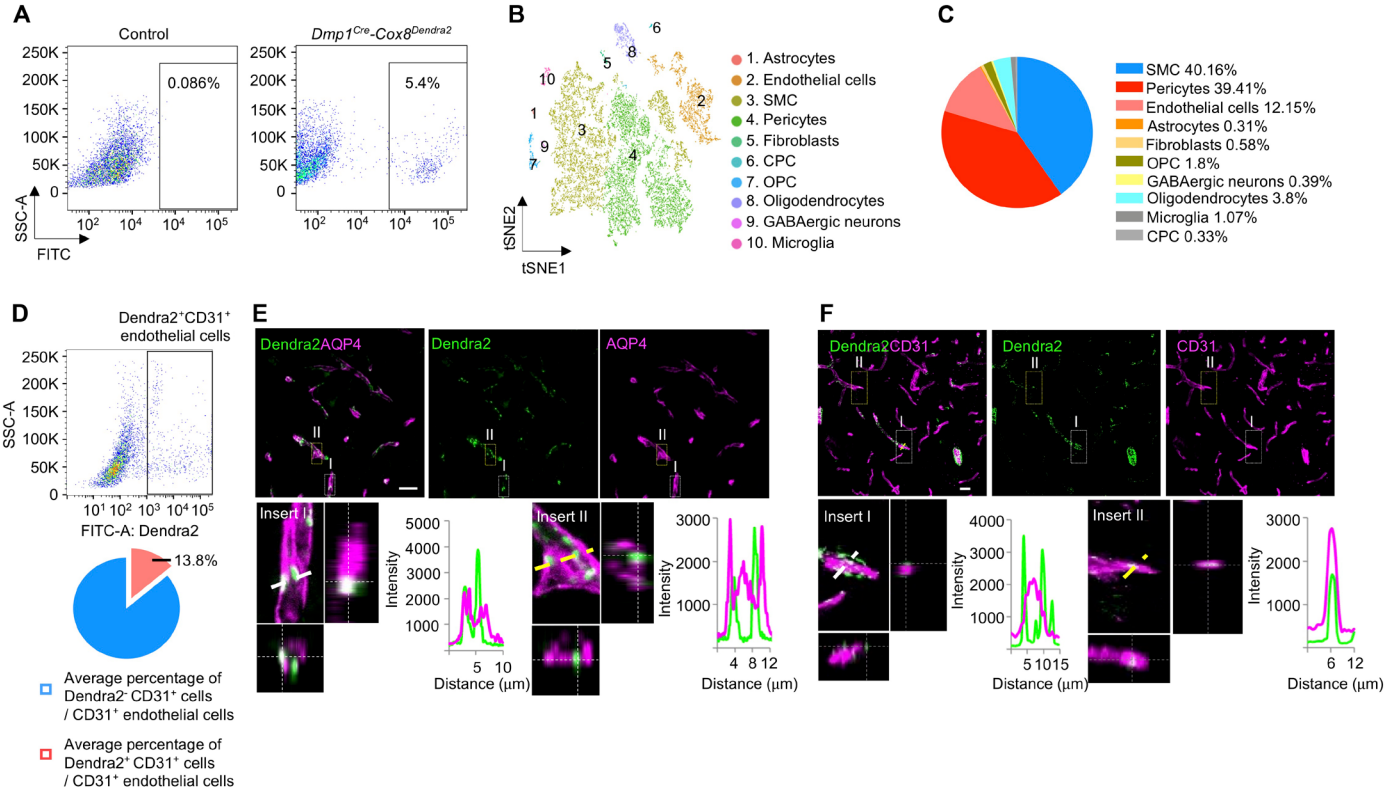

Fig. 3. Astrocytes^{Dmp1} transfer mitochondria to CECs in vivo. (**A**) Representative FACS plots for Dendra2-containing cells isolated from 1M male *Dmp1*^{Cre}-*Cox8*^{Dendra2} mouse brains ($n = 2$). Single cells isolated from age-matched male *Cox8*^{Dendra2} mouse brains were used as negative control ($n = 2$). (**B**) tSNE plot of reclustered *Dmp1*-negative cells from all Dendra2-containing cells ($n = 14,074$ cells) shows the cells that containing extrinsic mitochondria. (**C**) Pie diagram of the percentages of different Dendra2-containing *Dmp1*-negative cell types indicates the acquisition of extrinsic mitochondria in different cell types. (**D**) Representative scatter plot and pie diagram of the average percentage of Dendra2$^+$/CD31$^+$ endothelial cells among all CD31$^+$ endothelial cells in 1M male *Dmp1*^{Cre}-*Cox8*^{Dendra2} mouse brains ($n = 4$ mice). (**E**) Confocal images with orthogonal views and fluorescence intensity analysis of Dendra2 (refers to mitochondria of astrocytes^{Dmp1}) and astrocyte endfeet marker AQP4 in sagittal brain sections of 1M *Dmp1*^{Cre}-*Cox8*^{Dendra2} male mouse thalamus show Dendra2-labeled mitochondria colocalized with (insert I, white line) astrocyte endfeet or surrounded by (insert II, yellow line) astrocyte endfeet. Scale bar, 20 μm. (**F**) Confocal images with orthogonal views and fluorescence intensity analysis of Dendra2 (refers to mitochondria of astrocytes^{Dmp1}) and endothelial cell marker CD31 in 1M *Dmp1*^{Cre}-*Cox8*^{Dendra2} male mouse thalamus show Dendra2-labeled mitochondria aggregating around (insert I, white line) endothelial cells or colocalized with (insert II, yellow line) endothelial cells. Scale bar, 20 μm.

endfeet of astrocytes (Fig. 3E, insert I), as well as mitochondria adjacent to endfeet (Fig. 3E, insert II). Immunostaining of CD31 in *Dmp1*^{Cre}-*Cox8*^{Dendra2} mouse brain sections showed aggregation of mitochondria^{Dendra2} around CD31-labeled blood vessels (Fig. 3F, insert I) as well as the appearance of mitochondria^{Dendra2} within endothelial cells (Fig. 3F, insert II). Next, we conducted a bioinformatic comparison between endothelial cells from 1M WT and Dendra2-containing endothelial cells from 1M *Dmp1*^{Cre}-*Cox8*^{Dendar2} mouse brains in *Dmp1*-negative cell populations. This result revealed that endothelial cells received Dendra2-labeled mitochondria from astrocytes^{Dmp1} displaying up-regulated GO terms for cytoskeleton, adherens junction, and focal adhesion (fig. S6E). These results support the notion that CECs acquire mitochondria from local, adherent astrocytes^{Dmp1} in vivo.

Mitofusin 2–mediated mitochondrial transfer from astrocytes^{Dmp1} to endothelial cells decreases with age

Mitochondrial metabolism is closely related to aging, and our previous study showed that aging decreases intercellular mitochondrial transfer between osteocytes (*41*). We thus examined whether aging might also decrease mitochondrial transfer from astrocytes^{Dmp1} to endothelial cells in the brain. Using confocal imaging we compared fluorescent signals that marked mitochondria in the thalamus tissue between young and aged *Dmp1*^{Cre}-*Cox8*^{Dendra2} mice. We found that aging decreases the expression level of CD31 in brain thalamus (Fig. 4, A and B), where the total Dendra2 signals remain unchanged (Fig. 4, A and B). We observed a significant decrease of Dendra2 fluorescent signals from genetically labeled mitochondria of astrocytes^{Dmp1} cells that were colocalized with CD31-labeled endothelial cells as well as the percentage of colocalized Dendra2 signals among all Dendra2 fluorescent signals, in 20M aged mice as compared to 1M mice (Fig. 4, A and B). These results suggest that aging impaired the mitochondrial transfer efficiency from astrocytes^{Dmp1} to endothelial cells.

It has been reported that the enrichment of mitochondria at astrocyte endfeet and their contact with the ER is mediated by mitofusin 2 (MFN2), the critical ER-mitochondria tethering protein (*42*), and its expression in these cells is essential for vascular remodeling (*18*). Intriguingly, we reported that ER-mitochondria contact is fundamental for intercellular mitochondrial transfer between

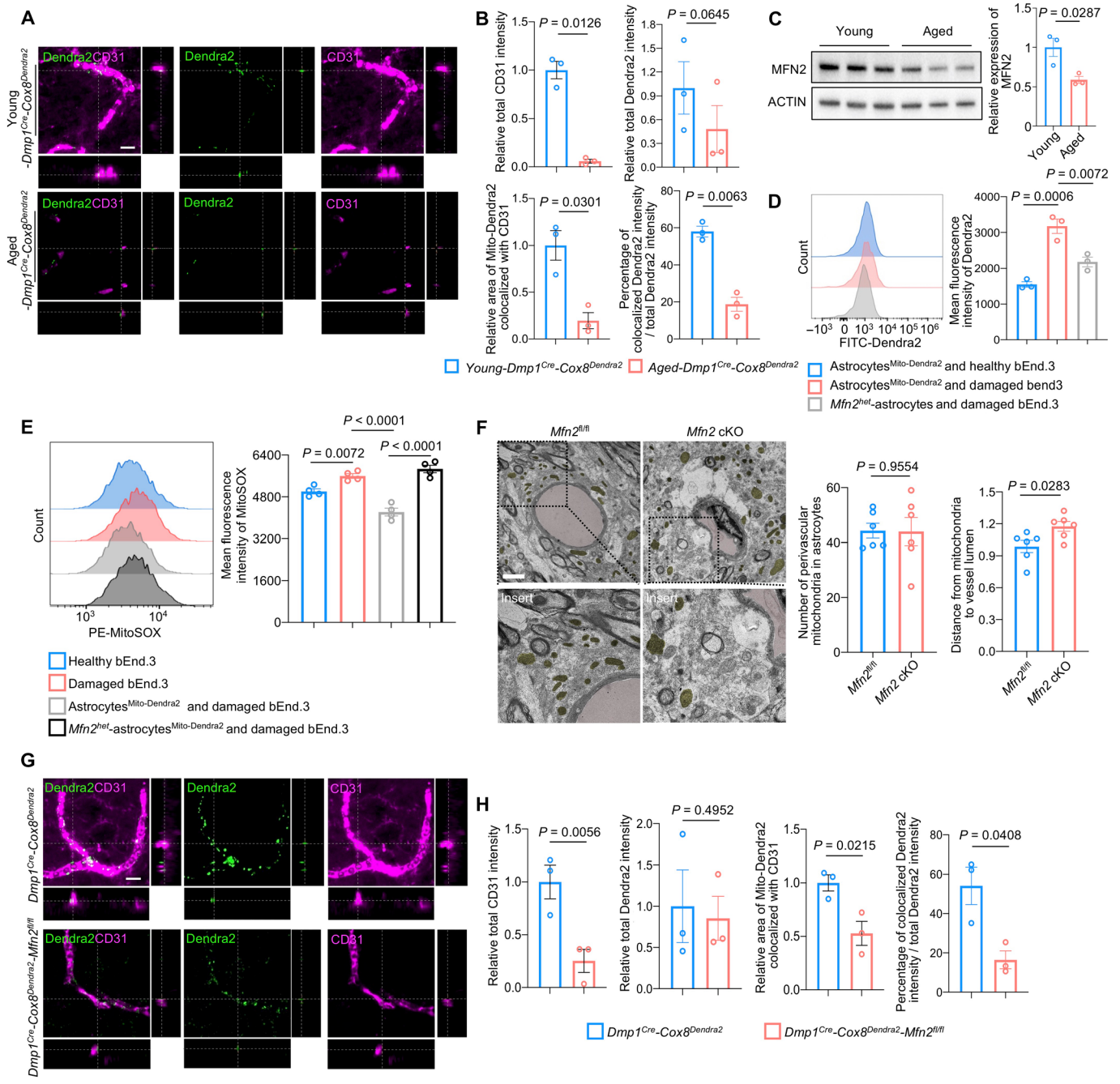

Fig. 4. MFN2-mediated mitochondrial transfer from astrocytes^{Dmp1} to endothelial cells decreases with age. (**A**) 3D confocal images of the Mito-Dendra2 and CD31-labeled endothelial cells within the thalamus of 1M young and 20M aged *Dmp1*^{Cre}-*Cox8*^{Dendra2} male mice. Scale bar, 10 μm. (**B**) Quantification of total CD31 intensity, area of Dendra2 colocalized with CD31, total Dendra2 intensity, percentage of CD31-colocalized Dendra2 intensity/total Dendra2 intensity from images in (A) ($n = 3$ mice per group). Two-tailed Student's paired *t* test. Data are presented as means ± SEM. (**C**) Images and quantification of immunoblotted MFN2 signal in thalamus tissues from 1M young and 20M aged WT mouse brains ($n = 3$ mice per group). Two-tailed Student's unpaired *t* test. Data are presented as means ± SEM. (**D**) Representative histogram overlays and quantification of Dendra2 intensity in healthy bEnd.3 cells cocultured with astrocytes$^{Mito\text{-}Dendra2}$, 2 μM A/R-damaged bEnd.3 cells cocultured with astrocytes$^{Mito\text{-}Dendra2}$ or *Mfn2*^{het}-astrocytes$^{Mito\text{-}Dendra2}$ ($n = 3$). One-way ANOVA followed by Tukey's post hoc test. Data are presented as means ± SEM. (**E**) Representative histogram overlays and quantification of MitoSOX intensity in healthy bEnd.3 cells, 2 μM A/R-damaged bEnd.3 cells, 2 μM A/R-damaged bEnd.3 cells cocultured with astrocytes$^{Mito\text{-}Dendra2}$ or *Mfn2*^{het}-astrocytes$^{Mito\text{-}Dendra2}$ ($n = 3$). One-way ANOVA followed by Tukey's post hoc test. Data are presented as means ± SEM. (**F**) Representative TEM images from the thalamus of 6w *Mfn2*$^{fl/fl}$ and *Mfn2*-cKO male mice and quantifications of the mitochondria (yellow) number in perivascular astrocyte endfeet and distance from mitochondrial outer membrane to capillary lumens (red) ($n = 6$ images from three mice per group). Scale bar, 2 μm. Two-tailed Student's unpaired *t* test. Data are presented as means ± SEM. (**G**) 3D confocal images of Dendra2-labeled mitochondria and CD31-labeled endothelial cells from the thalamus of 1M *Dmp1*^{Cre}-*Cox8*^{Dendra2} and *Dmp1*^{Cre}-*Cox8*^{Dendra2}-*Mfn2*$^{fl/fl}$ male mouse brains. Scale bar, 10 μm. (**H**) Quantification of total CD31 intensity, area of Dendra2 colocalized with CD31, total Dendra2 intensity, percentage of CD31-colocalized Dendra2 intensity/total Dendra2 intensity from images in (G) ($n = 3$ mice per group). Two-tailed Student's paired *t* test. Data are presented as means ± SEM.

osteocytes (*41*). Therefore, we speculated that MFN2 may mediate the transfer of mitochondria from astrocytes to endothelial cells in mice. By Western blotting, we found that MFN2 expression is decreased in the aged thalamus (Fig. 4C), in which astrocytes^{Dmp1} are abundant. We next induced astrocyte senescence by treating astrocytes with 500 μM hydrogen peroxide (H_2O_2) for 4 hours followed by 24 hours of normal culturing. By Western blotting of the cultured astrocytes, we found that H_2O_2 exposure resulted in an elevation of the senescence markers P53 and P19 (fig. S7A). Also, MFN2 expression level in astrocytes was significantly decreased after 500 μM H_2O_2 treatment (fig. S7A), revealing that astrocytes senescence is accompanied by disrupted MFN2 expression. To further validate whether aged astrocytes produce and transfer less extracellular mitochondria to endothelial cells, we conducted experiments to analyze the transfer efficiency of mitochondria from H_2O_2-treated astrocytes$^{Mito\text{-}Dendra2}$ to A/R-damaged endothelial cells. The results showed that though A/R-stressed endothelial cells incorporated more mitochondria from healthy astrocytes, the efficiency of incorporating astrocytes-derived mitochondria significantly decreased when A/R-stressed endothelial cells were cocultured with H_2O_2-induced senescent astrocytes$^{Mito\text{-}Dendra2}$ (fig. S7B). Next, to investigate the role of MFN2 in mediating mitochondrial transfer from astrocytes to endothelial cells, *CAG*^{Cre}-*Cox8*^{Dendra2}-*Mfn2*$^{fl/wt}$ mice were generated to obtain heterozygous *Mfn2* knockout (*Mfn2*^{het}) mice (fig. S7C). Then, primary cultures were prepared from *Mfn2*^{het} mouse brains to obtain primary *Mfn2*^{het}-astrocytes$^{Mito\text{-}Dendra2}$. Western blotting confirmed decreased MFN2 expression in primary *Mfn2*^{het}-astrocytes$^{Mito\text{-}Dendra2}$ compared with primary astrocytes$^{Mito\text{-}Dendra2}$ from *CAG*^{Cre}-*Cox8*^{Dendra2} mice (fig. S7D). To test whether MFN2 loss has an impact on astrocyte viability, proliferation, and mitochondrial gene expression profile, we conducted Cell Counting Kit-8 (CCK-8) assays and quantitative polymerase chain reaction (qPCR) on *Mfn2*^{het}-astrocytes and found that loss of MFN2 expression in astrocytes has no significant effect on cell viability (fig. S7E) nor on expression of genes related to cell proliferation (*Ki67*), mitochondrial adenosine triphosphate (ATP) synthesis (*mt-Atp6*), and mitochondrial biogenesis (*Pgc-1alpha*) (fig. S7F). Next, we pre-exposed bEnd.3 cells with 2/2 μM A/R treatment before conducting 3D Transwell coculturing with WT astrocytes$^{Mito\text{-}Dendra2}$ or *Mfn2*^{het}-astrocytes$^{Mito\text{-}Dendra2}$ for 24 hours (fig. S7G) before analysis. By flow cytometry analysis we found that A/R-treated damaged bEnd.3 cells triggered an increase of the fluorescence signal intensity of Dendra2-labeled mitochondria derived from astrocytes$^{Mito\text{-}Dendra2}$, but not from the *Mfn2*^{het}-astrocytes$^{Mito\text{-}Dendra2}$ (Fig. 4D), suggesting that heterozygous loss of *Mfn2* in astrocytes impaired mitochondrial transfer from astrocytes to endothelial cells. Further, we found that *Mfn2*^{het}-astrocytes$^{Mito\text{-}Dendra2}$ failed to alleviate ROS accumulation in endothelial cells as measured by MitoSOX when compared with WT astrocytes-Mito^{Dendra2} (Fig. 4E). Together, our results suggest that MFN2 mediates the transfer of functional mitochondria from astrocytes to endothelial cells.

Next, we investigated the effect of MFN2-mediated mitochondrial transfer from astrocytes^{Dmp1} to endothelial cells in vivo. We conditionally knocked out *Mfn2* in astrocytes^{Dmp1} by generating *Dmp1*^{Cre}-*Mfn2*$^{fl/fl}$ mice (*Mfn2*-cKO) (fig. S7H). TEM imaging on the thalamus of 6-week-old (6w) *Mfn2*$^{fl/fl}$ and *Mfn2*-cKO male mice revealed that loss of *Mfn2* in astrocytes^{Dmp1} increased the distance between astrocytic mitochondria and capillary lumens without affecting the number of perivascular mitochondria (Fig. 4F), suggesting that astrocytes^{Dmp1} in *Dmp1*^{Cre}-*Mfn2*$^{fl/fl}$ mice have a weakened capacity for mitochondrial transfer at perivascular astrocytic endfeet. To examine this further, we generated *Dmp1*^{Cre}-*Cox8*^{Dendra2}-*Mfn2*$^{fl/fl}$ fluorescent mice to trace the mobility of mitochondria in *Mfn2*-deleted astrocytes^{Dmp1} in vivo (fig. S7I). Confocal imaging of thalamus tissue and quantitation analysis revealed a significant decrease in fluorescent signal indicative of impaired mitochondrial transfer from astrocytes^{Dmp1} to CECs and reduced blood vessels (Fig. 4, G and H), whereas the total intensity of Mito-Dendra2 was not significantly changed, which presented a similar feature of aged mice (Fig. 4, A and B). In addition, to study whether DMP1 regulates Mfn2 expression in astrocytes, we compared the gene expression level of *Mfn2* between *Dmp1*$^{+}$ and *Dmp1*$^{-}$ astrocytes, but the result showed a nonsignificant difference between them (fig. S8A). Further investigation revealed that the protein level of MFN2 is not significantly changed in DMP1-stimulated astrocytes (fig. S8B). In addition, we performed the flow cytometry analysis of mitochondrial transfer efficiency in vitro under the stimulation of DMP1 protein, and the results indicate that different concentrations of DMP1 stimulation on astrocytes did not alter the efficiency of mitochondrial transfer from astrocytes to endothelial cells in our in vitro coculture system (fig. S8C). In summary, these results indicate that MFN2 mediates mitochondrial transfer from astrocytes^{Dmp1} to endothelial cells and that the decreased MFN2 in astrocytes contributes to the age-associated decrease of mitochondrial transfer efficiency.

Deletion of *Mfn2* in astrocytes^{Dmp1} leads to BBB disruption

To further investigate the effect of MFN2-mediated mitochondrial transfer from astrocytes^{Dmp1} on blood vessels, we performed scRNA-seq of single-cell suspensions prepared from the brains of 6w *Mfn2*-cKO male mice ($n = 3$) and corresponding, age-matched WT ($n = 3$) male mice. After quality control (see Materials and Methods), 10,366 cells from *Mfn2*-cKO mouse brains and 5982 cells from WT mouse brains were sequenced and analyzed before cells were identified and clustered into known lineages, according to the marker genes of different cell types: oligodendrocytes, microglia, CPCs, endothelial cells, erythrocytes, macrophages, T cells, immature neurons, monocytes, astrocytes, B cells, fibroblasts, neutrophil, ependymal cells, glutamatergic neurons, pericytes and neuronal-restricted precursors (fig. S9, A to D). Next, by GO analysis we found a significant down-regulation of genes related to angiogenesis, blood vessel remodeling, blood vessel development, and vasculogenesis in *Mfn2*-cKO mice endothelial cells (Fig. 5A). Gene set enrichment analysis (GSEA) in the context of *Mfn2* deletion in astrocytes^{Dmp1} also documented inhibition of angiogenesis and blood vessel development (Fig. 5B). By comparing the differentially expressed genes, we also observed that genes contributing to BBB integrity, such as the endothelial tight junction (*Cldn5*) (*43*) and basement membrane (*Col4a1*) (*44*), were significantly down-regulated in the endothelial cells of *Mfn2*-cKO mice (Fig. 5C). To further study the change of essential blood vessel characteristics in *Mfn2*-cKO mouse brain endothelial cells at the level of single samples, we then applied the computational single-sample gene set enrichment analysis (ssGSEA). We found that the cellular activities, such as bicellular tight junction assembly and endothelial migration, were significantly decreased in endothelial cells of *Mfn2*-cKO mouse brains (Fig. 5D), activities of which are relevant to the establishment of BBB, as well as to angiogenesis and branching activities for blood vessels (Fig. 5E). In summary, these results

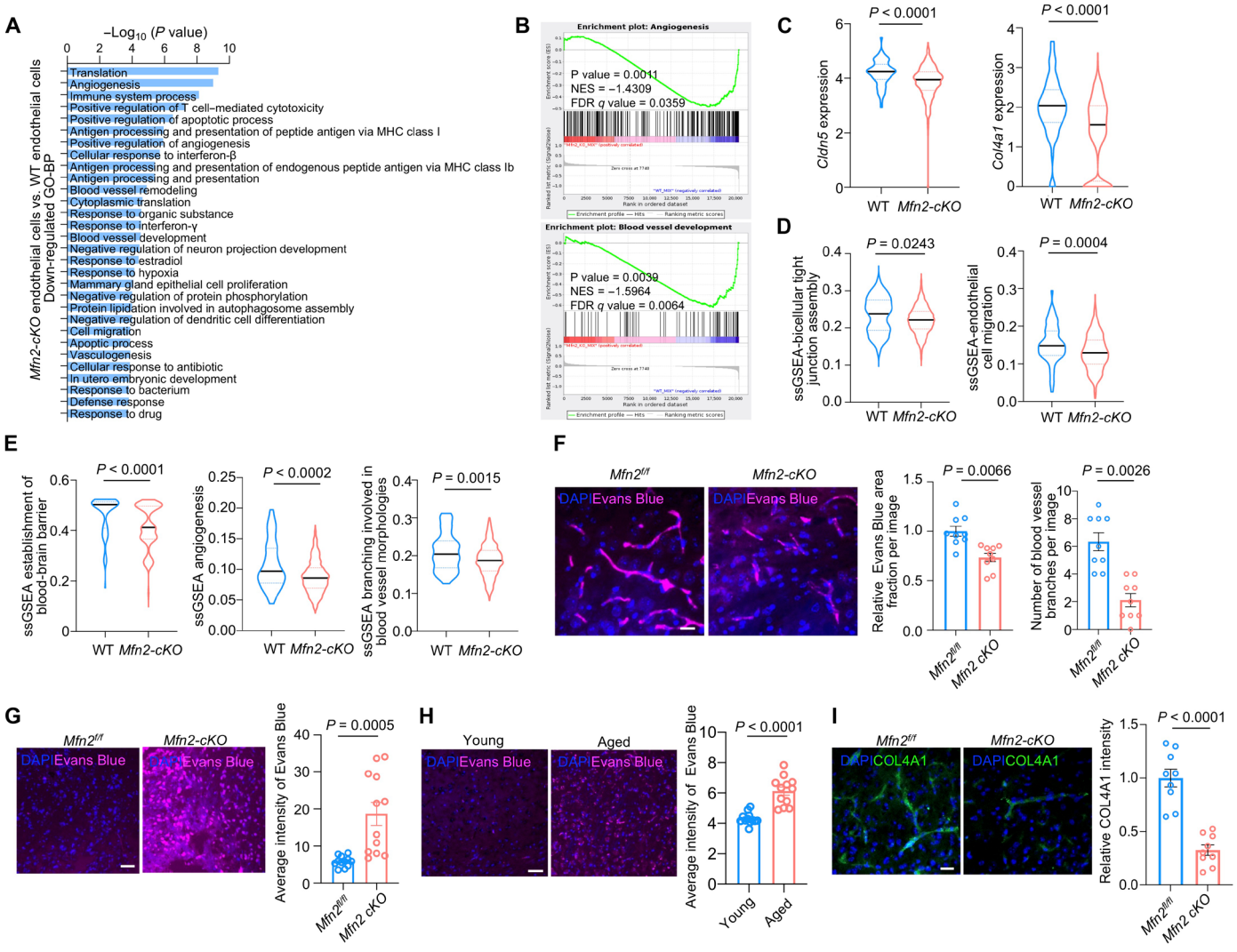

Fig. 5. Deletion of *Mfn2* in astrocytes^{Dmp1} leads to BBB disruption. (**A**) The top 30 significantly down-regulated GO enrichment terms of biological process in *Dmp1*-negative endothelial cells of *Mfn2*-cKO mice compared with that of WT mice. (**B**) GSEA of *Dmp1*-negative endothelial cells for angiogenesis and blood vessel development in *Mfn2*-cKO mice compared with WT mice. (**C**) Gene expression level of *Cldn5* and *Col4a1* between WT and *Mfn2*-cKO mice *Dmp1*-negative endothelial cells. Wilcoxon rank sum test. Data are presented as median. (**D** and **E**) Comparisons between WT and *Mfn2*-cKO mice *Dmp1*-negative endothelial cells for ssGSEA on bicellular tight junction assembly and endothelial migration (D), and establishment of BBB, angiogenesis, and branching involved in blood vessel morphologies (E). Wilcoxon rank sum test. Data are presented as median. (**F**) Representative images and quantification of Evans Blue–filled blood vessel density and the number of vessel branches in the thalamus capillaries of 1M *Mfn2*$^{fl/fl}$ and *Mfn2*-cKO male mice ($n = 9$ images from three mice for each group). Scale bar, 20 μm. Two-tailed Student's paired *t* test. Data are presented as means ± SEM. (**G**) Representative images and quantification of the leaked Evans Blue dye fluorescence intensity in the thalamus of *Mfn2*$^{fl/fl}$ and *Mfn2*-cKO 1M male mouse brains ($n = 12$ captured image areas from three mice for each group). Scale bar, 50 μm. Two-tailed Student's unpaired *t* test. Data are presented as means ±SEM. (**H**) Representative images and quantification of the leaked Evans Blue dye fluorescence intensity in the thalamus of young (1M) and aged (20M to 22 M) WT mouse brains ($n = 12$ captured image areas from three mice for each group). Scale bar, 50 μm. Two-tailed Student's unpaired *t* test. Data are presented as means ± SEM. (**I**) Representative images and the quantification of COL4A1 intensity in the thalamus of 1M *Mfn2*$^{fl/fl}$ and *Mfn2*-cKO male mouse brains ($n = 9$ images from three mice for each group). Scale bar, 20 μm. Two-tailed Student's paired *t* test. Data are presented as means ± SEM.

demonstrate that loss of *Mfn2* in astrocytes^{Dmp1} causes the reduction of angiogenic and vessel assembly activities.

Next, we investigated whether *Mfn2* deletion in astrocytes^{Dmp1} changes blood vessel density. Fluorescent Evans Blue dye was injected into animals without perfusion, and tissue sections were prepared. We found a significant reduction in blood vessel density and branch number in the thalamus of *Mfn2*-cKO mice (Fig. 5F). To examine whether deletion of *Mfn2* in astrocytes^{Dmp1} influences BBB permeability, the Evans Blue dye leakage test by both confocal imaging and high-throughput spectroscopy after trichloroacetic acid (TCA) treatment were used. The results showed that the dye leakage was significantly increased in the thalamus regions of *Mfn2*-cKO mice compared with corresponding control *Mfn2*$^{fl/fl}$ samples (Fig. 5G and fig. S10A). Consistent with this observation of decreased MFN2 expression in aged mice, aged mice displayed poor BBB integrity in the thalamus as evidenced by the leakage of Evans Blue dye (Fig. 5H and fig. S10B).

Furthermore, Collagen IV (COL4A1), the most abundant component of basement membrane that contributes to BBB integrity (*44*), was also significantly reduced in the thalamus of *Mfn2*-cKO mice (Fig. 5I). Together, these results indicate that MFN2-deficiency in astrocytes^{Dmp1} links the impaired mitochondrial transfer between astrocytes^{Dmp1} and endothelial cells to age-related BBB breakdown.

Astrocyte-derived mitochondria restore endothelial dysfunction

To examine the role of astrocyte-derived mitochondria in endothelial cells, and to exclude potential confounding factors secreted by astrocytes, such as hormones or growth factors, we next isolated active mitochondria from primary WT astrocytes and transplanted them into bEnd.3 cells directly according to reported instructions (*45*). By confocal imaging analysis, we found that mitochondria isolated from primary astrocytes$^{Mito\text{-}Dendra2}$ are active, as evidenced by staining of the mitochondrial membrane potential–dependant dye MitoTracker Red (MTR) CMXRos (fig. S11A). Next, we coincubated these active mitochondria isolated from astrocytes$^{Mito\text{-}Dendra2}$ with bEnd.3 endothelial cells. Protein quantification based on the bicinchoninic acid (BCA) protein assay kit showed an approximate concentration of 850 μg/ml of the 100-μl mitochondrial suspension isolated from 1,000,000 astrocytes. With increasing the volume (21.25, 42.5, and 85 μg, respectively) of mitochondria isolated from donor cells (primary astrocytes$^{Mito\text{-}Dendra2}$), we found that the numbers of internalized mitochondria in bEnd.3 cells after 24 hours of coincubation were improved (fig. S11, B and C). To determine whether astrocytes-derived mitochondria can alleviate endothelial oxidative stress in bEnd.3 cells, we treated bEnd.3 cells with 2/2 μM A/R, followed by transplantation with mitochondria from primary WT astrocytes (Fig. 6A). Following further incubation for 24 hours before analysis by flow cytometry, we found that 21.25 μg of mitochondria isolated from astrocytes significantly rescued the A/R-induced ROS (H_2DCFDA) stress of bEnd.3 endothelial cells (Fig. 6B). Quantitative analysis showed that the ROS level in stressed bEnd.3 cells could be lowered to a normal level after improving the number of transplanted mitochondria to 42.5 μg (Fig. 6B), with no further rescue effect at the higher amount of 85 μg of mitochondria (Fig. 6B).

To confirm the effect of astrocyte-derived mitochondria on endothelial functions, we sequenced bulk RNA from bEnd.3 endothelial cells with or without astrocytes-derived mitochondrial

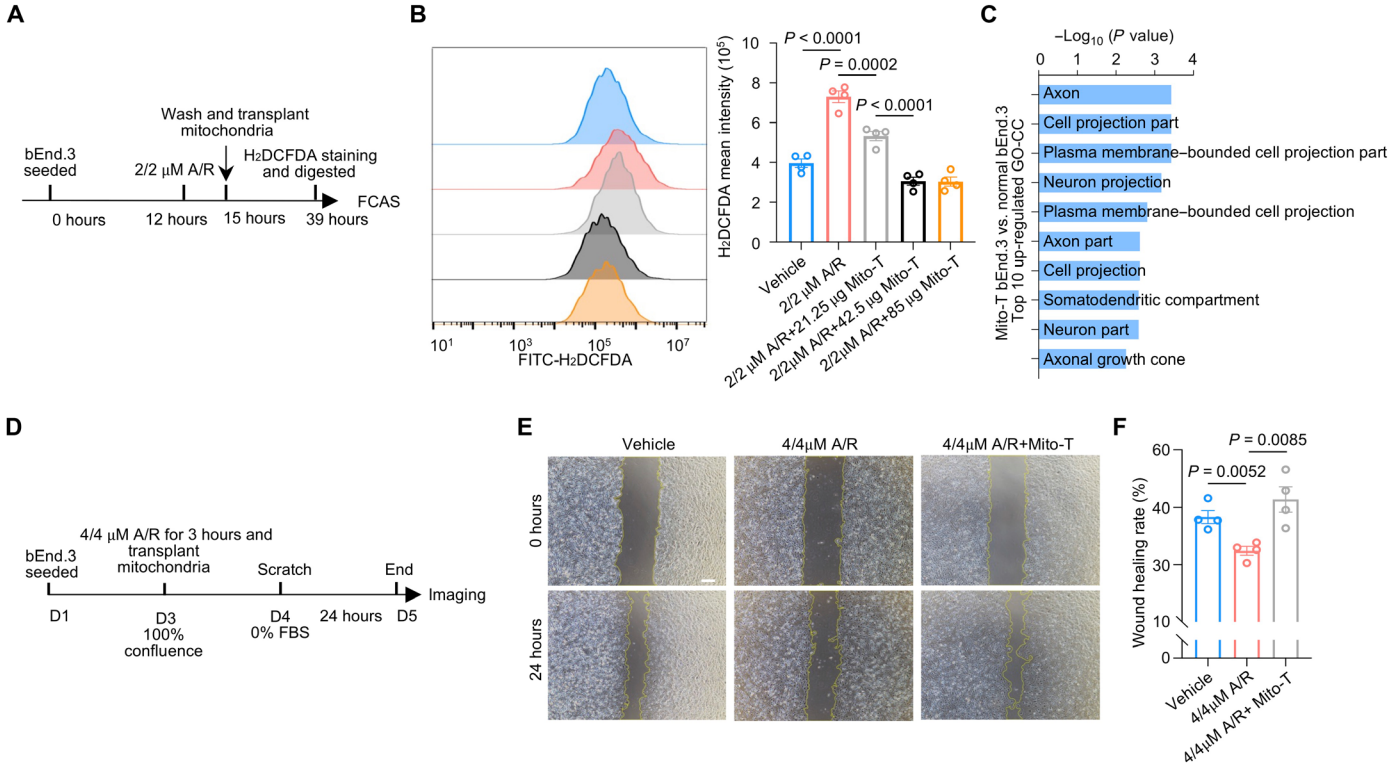

Fig. 6. Astrocytes-derived mitochondria restore endothelial dysfunction. (**A**) Work flow of 2/2 μM A/R treatment on bEnd.3 endothelial cells followed by mitochondrial transplantation and H_2DCFDA staining for flow cytometry analysis. (**B**) Representative histogram overlays and quantitative results of ROS (H_2DCFDA) intensity in healthy (vehicle), 2/2 μM A/R-damaged bEnd.3 endothelial cells, and 2/2 μM A/R-damaged bEnd.3 endothelial cells after transplanted with 21.25-, 42.5-, and 85-μg astrocytes-derived mitochondria (Mito-T) ($n = 4$). One-way ANOVA followed by Tukey's post hoc test. Data are presented as means ± SEM. (**C**) Top 10 up-regulated GO enrichment terms of cellular components (CC) in bEnd.3 cells transplanted with primary WT astrocytes-derived mitochondria compared with normal control bEnd.3 cells. (**D**) Workflow for 4/4 μM A/R treatment on bEnd.3 endothelial cells followed by mitochondrial transplantation and cell scratch assay. (**E**) Representative images of scratched bEnd.3 endothelial cells without A/R treatment (vehicle), with 4/4 μM A/R treatment, with 4/4 μM A/R treatment and subsequent transplantation of approximately 170 μg of mitochondria isolated from primary astrocytes (up panel), followed by 24 hours of normal culture (below panel). Scale bar, 200 μm. (**F**) Quantification of wound healing rate after 24 hours of normal culture in bEnd.3 endothelial cells without 4/4 μM A/R treatment (vehicle), with 4/4 μM A/R treatment, with 4/4 μM A/R treatment and subsequent transplantation of approximately 170 μg of mitochondria ($n = 4$). One-way ANOVA followed by Tukey's post hoc test. Data are presented as means ± SEM.

supplementation. We found that the top 10 up-regulated GO terms were indicative of a strong capacity for forming cell membrane projections in bEnd.3 cells that acquired mitochondria from astrocytes (Fig. 6C). Endothelial cell migration is an essential process for angiogenesis (*46*) and also represents a feature for cells that form the BBB (*47*, *48*). To model this cellular behavior in vitro, we next conducted a cell scratch and wound healing assay to evaluate the effect of mitochondrial supplementation on cell migration by bEnd.3 cells (*49*). Treatment with increasing concentrations of A/R significantly decreased the wound healing rate, with a minimum threshold effect at 4/4 μM exposure of A/R (fig. S12, A and B). With this finding, we performed a mitochondrial transplantation assay in the presence of 4/4 μM A/R–treated bEnd.3 endothelial cells (Fig. 6D). Supplementation of astrocyte-derived mitochondria effectively restored the cell migration of A/R-treated endothelial cells (Fig. 6, E and F). Together, our results indicate that the intercellular transfer of mitochondria from astrocytes^{Dmp1} to endothelial cells of the BBB sustains endothelial homeostasis, protects against endothelial dysfunction, and promotes angiogenesis.

DISCUSSION

In this study, we showed astrocytes that express *Dmp1* specifically are associated with BBB integrity. They extend a strong endfeet structure to wrap around blood vessels and transfer mitochondria to CECs (fig. S13). Depletion of the ER-mitochondria contact protein, MFN2, in astrocytes^{Dmp1} curtails mitochondrial transfer activity and leads to BBB leakage. Disruption of this mitochondrial transfer process is associated with age-related BBB integrity. Together, these studies collectively demonstrate the functional relevance of intercellular mitochondrial transfer from astrocytes to endothelial cells is crucial in the CNS during homeostasis and aging.

In the CNS, mitochondrial cross-talk between astrocytes and neurons has been well-documented (*50*–*52*). Astrocytes facilitate mitochondrial transfer into neurons to rescue neuronal damage after stroke (*50*). Here, we provided a finding that astrocytes also transfer mitochondria to CECs to mediate BBB integrity and angiogenic function. Our study at least in part explains why an increase of damaged mitochondria in the astrocytic endfeet of patients with idiopathic intracranial hypertension (*53*) have BBB leakage (*54*). In mammalian cells, MFN2 is an inherent outer mitochondrial membrane guanosine triphosphatase that mediates mitochondrial fusion as well as mitochondrial interaction with ER under physiological conditions (*55*). We have previously reported that MFN2 is required for mediating the transfer of mitochondria between osteocytes dendritic network under physiological condition (*41*). In astrocytes, MFN2 has also been shown to increase the "polarized" distribution of ER-mitochondria tethering at astrocytes endfeet specifically for angiogenesis and vascular remodeling (*18*). Notably, the results reported by Gbel *et al.* implied that *Mfn2* deletion in astrocytes did not visibly affect astrocytes mitochondrial cristae morphology, cristae intactness, and abundance of ER tubules with a nonsignificantly altered metabolic profile. Furthermore, the ingenuity pathway analysis of their proteomic dataset disclosed that lack of MFN2 brings about only a modest mitochondrial dysfunction (*18*), which raised the question of how changes of ER-mitochondria contact in astrocytes influenced vascular regeneration. Astrocytes have been reported to be capable of extruding their mitochondria within extracellular vesicles (*50*, *56*, *57*), and ER-mitochondrial interactions are important for reinforcing mitochondrial energy production and redox homeostasis during the process of astrocyte-derived mitochondrial transfer (*57*). In the context of such findings by others, our results suggest that though MFN2 loss does not significantly influence the astrocytes viability, proliferation, ATP synthesis, and mitochondrial biogenesis, the capability of transferring mitochondria to CECs is remarkably inhibited, resulting in a breakdown of BBB integrity. Our current study showed another specific role of MFN2 in astrocytes by mediating the mitochondrial cross-talk from astrocytes to endothelial cells. Together, these evidence imply that MFN2 plays a role in astrocytes by mediating mitochondrial motility under naïve conditions. Though aging might also induce mitochondrial stress in endothelial cells, which was shown as a trigger of mitochondrial transfer from astrocytes, we also showed that aging and senescence in astrocytes decrease MFN2 expression as well as the attenuated mitochondrial transfer efficiency. We speculate that though the mitochondrial ROS stress in aged endothelial cells may trigger mitochondrial transfer, the attenuated MFN2 level in aged astrocytes can still result in the decreased mitochondrial incorporation to endothelial cells in the brain. Considering that astrocytic dysfunction may cause deleterious effects on adjacent cells (*58*), and that the regulation of BBB structures is complex, there could be other factors potentially contribute to the deleterious vascular effect apart from MFN2. For example, the secretion of apolipoprotein E from astrocytes has significant impact on the signaling transmission in pericytes, which might also contribute to BBB breakdown (*59*). In addition, the Dmp1 mutant has been reported to disrupt endfeet (*39*), resulting in the reduction of astrocytic coverage on blood vessels and the molecular signaling within the BBB unit. It is probable that DMP1 helps maintain endfeet coverage for MFN2-mediated mitochondrial transfer between astrocytes and endothelial cells, while we cannot determine whether MFN2 loss has an effect on DMP1 functions at this stage. Other factors, such as intracellular calcium signaling within astrocytes or the intercellular calcium propagation between astrocytes and vascular cells through gap junctional pathway/purinergic pathway, might also contribute to deleterious effects on the cerebrovascular system (*60*, *61*).

As the essential cellular component of the BBB, CECs are vulnerable to functional impairment in CNS-related disorders, such as stroke (*23*), brain injury (*62*), neurodegenerative disease (*63*), as well as aging (*64*). Throughout life, CECs endure constant endogenic or ectogenic mitochondrial stress that results in ROS accumulation (*23*). Lee *et al.* reported the deletion of CR6-interacting Factor1 (Crif1), a mitochondrial protein involved in the synthesis and insertion of oxidative phosphorylation (OXPHOS) peptides, compromised ATP production in CECs and thus resulted in the reorganization of the actin cytoskeleton, a decrease of tight junction–associated proteins expression, and increase of BBB permeability (*24*), suggesting the crucial role of mitochondria in regulate CEC functions. Our understanding of mitochondrial transfer from astrocytes to CECs has paved the way for the development of mitochondrial transplant therapy as a potential treatment for CNS disorders by rebuilding mitochondrial homeostasis. It is intriguing that in the reported studies of intercellular mitochondrial transport within CNS, astrocytes appear as the dominant participants that act as the donors to deliver mitochondria to other cells (*50*, *51*, *65*). Notably, the extrusion of mitochondria from astrocytes to damaged neurons amplifies the cell survival signals in neurons and thus contributes to

post-stroke recovery (*50*), which is developing as a promising strategy to alleviate stroke. A recent study demonstrated the transfer of mitochondria from astrocytes to glioblastoma cells appears as a prevalent event that enhances glioblastoma tumorigenesis in brain (*66*), which further reinforced the perception that astrocytes might act as a mitochondrial reservoir within the CNS to maintain the mitochondrial homeostasis of the regional microenvironment. The defect of astrocytes^{Dmp1} or endothelial cells in other models of CNS-related disorders, such as dementia, hypertension encephalopathy, or trauma, deserves further studies to explore insights into the breakdown of the BBB and imbalanced mitochondrial homeostasis. Using endothelial wound healing and endothelial cell migration assays as features of BBB homeostasis (*47*, *48*), our study showed the mitochondria isolated from astrocytes can restore endothelial crises in the BBB. For future applications, it is meaningful to develop efficient mitochondrial transplantation methods to improve the efficiency of mitochondrial transplantation in both in vitro and in vivo conditions to develop ideal therapeutic strategies. The appropriate modifications on isolated mitochondria should be considered to improve the vitality, efficiency, and feasibility of mitochondrial transplantation. It is expected to apply some chemical or physical strategies to optimize the process of mitochondrial delivery and to take full advantages of the astrocytes-derived mitochondria in rescuing endothelial dysfunctions as well as cerebrovascular disorders.

Astrocytes are found extensively across cerebral tissues and are highly heterogeneous in appearance and function and in their location-specific gene expression signatures (*14*, *15*). Evidence also exists that positionally distinct astrocytes are derived from different progenitors (*67*, *68*). Recent work has reported on the broad contact of astrocytes with vessels in the cortex/gray matter (*69*). However, investigations on the spatial distribution, as well as the morphological diversity, of all astrocytes are heavily dependent on different labelling/imaging methods and experimental conditions. Considering the strong heterogeneity of astrocytes, subtype selectivity by different astrocyte markers might lead to labelling bias that will give different conclusions. DMP1 is a noncollagenous, acidic extracellular matrix protein that plays a critical role in the mineralization of hard tissues such as bone and dentin (*70*–*72*). Accompanied with the unraveling of the protein property and structure, accumulating evidence has revealed the various functions of DMP1 other than mineralization. Previous study showed that astrocytes DMP1 promotes cell adhesion between astrocytes and vascular endothelial cells by organizing the extracellular matrix components of BBB structures, including laminins, collagens, integrins, and chondroitin sulfate proteoglycan (*39*). Particularly, mutation of DMP1 expression significantly disrupted AQP4 expression and perivascular endfeet structure of astrocytes, suggesting that DMP1 also plays a critical role in maintaining polarized terminal processes of astrocytes to encase blood vessel (*39*). Consistent with the literature, our study identifies a population of *Dmp1*-expressing astrocytes that highly adhere to endothelial cells and have the strong perivascular endfeet structure necessary for transferring mitochondria to endothelial cells. In short, we showed that *Dmp1*-expressing astrocytes transfer mitochondria to endothelial cells of the BBB to sustain endothelial homeostasis. We have provided important insights into the designing of mitochondrial transfer to maintain lifelong BBB function in health and disease.

Limitations of the study

The current study has several limitations and also suggests several outlooks for future research. First, though FACS enrichment for scRNA-seq is a widely used method to identify the cell types and transcriptomics in specific cell populations (*73*), the process of sorting for a specific cell proportion can sometimes be influenced by uncontrollable sorting-related issues, such as time length, harsh damage and random variation during cell sorting, especially for heterogeneous tissues (*74*–*76*). The output of FACS has a limitation of precisely measuring the subcellular distribution of fluorescence in vivo (*77*). While our scRNA-seq on whole-brain of WT mice has shown the dominant expression of *Dmp1* is in astrocytes, which is consistent with the major proportion of *Dmp1*$^+$ cell types, the FACS enrichment in our study indeed suggests that a proportion of fluorescence-sorted cells did not reflect the real proportion of *Dmp1*$^+$ cells in vivo. Nevertheless, the purpose of this Dendra2-sorting scRNA-seq is to identify the cell types of the *Dmp1*-negative cell population, which is considered as mitochondrial recipient cells. As we showed, astrocytes are the major cell types of *Dmp1*$^+$ cells, that can transfer Dendra2-labeled mitochondria to endothelial cells in vivo. And our further in vitro coculture experiments validated the transfer of mitochondria from astrocytes to endothelial cells. However, because we also found that SMCs comprise a small proportion (13.58%) of *Dmp1*$^+$ cells, the current work cannot completely exclude the potential possibility that these *Dmp1*$^+$ SMCs, could also contribute to the process of transferring mitochondria to endothelial cells. In the brain, capillaries that lack the embrace by SMCs on the abluminal surface of blood vessels, make up 85% of the vasculature and are the principal contributors to BBB function (*78*). Though the mitochondrial transfer from *Dmp1*$^+$ SMCs to endothelial cells might occur and mediate endothelial functions as well, the influence on our conclusions that *Dmp1*-expressing astrocytes mediate endothelial functions and BBB via mitochondrial transfer is limited.

Second, the transcriptional analysis of *Dmp1*$^+$ cells and the FACS enrichment for scRNA-seq also indicate that SMCs and pericytes also acquired extrinsic mitochondria. In this study, we could not determine or exclude the possibility that astrocytes also transfer mitochondria to SMCs or pericytes. As one of the cell types that contain abundant mitochondria, vascular SMCs rely on mitochondrial metabolism to modulate cell growth, proliferation, contraction, as well as the blood flow (*79*, *80*) and thus also contribute to the integrity of BBB (*81*). On the other hand, pericytes regulate BBB mainly by regulating BBB-specific gene expression patterns in endothelial cells (*82*). Considering the complexity of BBB components, it is not clear how these SMCs and pericytes could also contribute to the maintenance of BBB integrity. In addition, it remains unknown whether astrocytes^{Dmp1} MFN2 also mediates the potential transfer of mitochondria to SMCs/pericytes, which could act as the intermediary target to mediate endothelial cells and BBB integrity.

Third, aging is a complicated process accompanied with vigorous pathological changes and degenerations, and the decreased mitochondrial transfer in aged mice might not be solely attributed to the changes of MFN2 levels alone. Future studies are expected to validate the correlation between the MFN2 alteration in astrocytes during aging and the transport of mitochondria to endothelial cells, such as replenishing MFN2 in aged mice, which may represent relevant tools for the recovery of defective mitochondrial transport in different neurovascular diseases as well as aging.

MATERIALS AND METHODS

Animal models

Cox8^{Dendra2} [B6;129SGt(ROSA)26Sor$^{tm1(CAG-COX8A/Dendra2)Dcc}$/J, stock number: 018385] and Mfn2$^{fl/fl}$ [B6.129(Cg)-Mfn2^{tm3Dcc}/J, stock number: 026525] and Ai9 [B6.Cg-Gt(ROSA)$^{26Sortm9(CAG-tdTomato)Hze}$/J, stock number: 007909] mice lines were purchased from the Jackson Laboratory. CAG^{Cre} [B6/JGpt-Tg(CAG-Cre)/Gpt, stock number: T004055] and mGmT [B6/JGpt-H11$^{em1Cin(CAG-LoxP-ZsGreen-Stop-LoxP-tdTomato)}$/Gpt, stock number: T006163], and C57BL/6 J (WT) [stock number: N000013] mouse strains were purchased from GemPharmtech Co.,Ltd. The 9.6-kb *Dmp1^{Cre}* transgenic mice were provided by J. Q. (Jerry) Feng at Texas A&M College of Dentistry, USA (*83*). All animals were housed in a specific pathogen–free facility under standard conditions. Animal experimental procedures were performed in accordance with the Institutional Animal Care and Use Committee guidelines and approved by the Animal Care and Use Committee of Shanghai Jiao Tong University Affiliated Sixth People's Hospital (China).

Cell culture

Primary WT astrocytes or transgenic astrocytes for Dendra2 expression in mitochondria (Mito-Dendra2) were isolated from whole brains of WT, *CAG^{Cre}-Cox8^{Dendra2}*, or *Mfn2^{het}* 3- to 4-day-old neonatal mice following accepted guidelines (*84*). Briefly, brain tissues were first mechanically dissociated by pipets and then digested in 0.25% trypsin in a water bath at 37°C for 15 min with occasional shaking every 5 min. Digested brain tissues were then dissociated into single cells by adding an equal volume of high-glucose Dulbecco's modified Eagle's medium (DMEM) containing 10% fetal bovine serum (FBS) and 1% penicillin/streptomycin (P/S). After several times of vigorous pipetting, dissociated single-cell suspensions were then sequentially filtered by a 100- and 70-μm cell strainer respectively to remove clumps. Following 400*g* centrifugation for 5 min and removal of red cells, cell suspension was plated and cultured in high-glucose DMEM supplemented with 10% FBS and 1% P/S at 37°C with 5% CO_2. After a complete change of the culture medium at 24 hours and regularly changing the medium every 3 days, culture flasks with confluent astrocytes were shaken at 240 rpm for 6 hours on day 7 or 8 to remove microglia and OPCs. The remaining attached astrocytes were then passaged for further use, and all astrocytes were used within five passages (P5).

Mouse brain microvascular endothelial cell line bEnd.3 (American Type Culture Collection) were cultured in high-glucose DMEM containing 10% FBS and 1% P/S at 37°C with 5% CO_2. All used bEnd.3 cells were cultured within 30 passages (P30).

scRNA-seq and analysis

Single-cell dissociation

scRNA-seq experiments were performed by NovelBio Bio-Pharm Technology Co., Ltd. Tissues for analysis were dissected and kept in MACS Tissue Storage Solution (Miltenyi Biotec) until processing. Briefly, samples were first washed with phosphate-buffered saline (PBS), minced into small pieces (approximately 1 mm^3) on ice and enzymatically digested with papain (200 U/ml; Diamond) and cysteine-HCl (Sigma-Aldrich) for 45 min at 37°C, with agitation. After digestion, samples were sieved through a 40-μm cell strainer and centrifuged at 300*g* for 50 min. After removing the supernatant, the pelleted cells were resuspended in red blood cell lysis buffer (Miltenyi Biotec) to lyse red blood cells. After washing with PBS containing 0.04% bovine serum albumin (BSA), the cell pellets were resuspended in PBS containing 0.04% BSA and refiltered through a 35-μm cell strainer. For the Dendra2 sorting and enrichment for sequencing, brains from 1M *Dmp1^{Cre}-Cox8^{Dendra2}* male mice ($n = 2$) were dissociated into single cells according to methods described above. The Dendra2-containing cells were then sorted on a BD FACSMelody (BD Bioscience) using the manufacturer's recommended settings. Dissociated single cells were then stained with acridine orange/propidium iodide (AO/PI) for viability assessment using Countstar Fluorescence Cell Analyzer. The single-cell suspension was further enriched with a MACS dead cell removal kit (Miltenyi Biotec) before sequencing.

Single-cell sequencing

The scRNA-seq libraries were generated using the 10× Genomics Chromium Controller Instrument and Chromium Single Cell 3' V3.1 Reagent Kits (10× Genomics, Pleasanton, CA). Briefly, cells were concentrated to 1000 cells/μl and loaded into each channel to generate single-cell Gel Bead-In-Emulsions (GEMs). After the reverse transcription step, GEMs were broken, and barcoded-cDNA was purified and amplified. The amplified barcoded cDNA was fragmented, A-tailed, ligated with adaptors and index PCR amplified. The final libraries were quantified using the Qubit High Sensitivity DNA assay (Thermo Fisher Scientific), and the size distribution of the libraries was determined using a High Sensitivity DNA chip on a Bioanalyzer 2200 (Agilent). All libraries were sequenced by illumina sequencer (Illumina, San Diego, CA) on a 150-bp paired-end run.

Single-cell RNA statistical analysis

scRNA-seq data analysis was performed by NovelBio Bio-Pharm Technology Co.,Ltd. using a NovelBrain Cloud Analysis Platform. We applied fastp with default parameter filtering the adaptor sequence and removed the low-quality reads to achieve clean data (*85*). Next, feature-barcode matrices were obtained by aligning reads to the human genome (GRCm38 Ensemble: version 92) using CellRanger v3.1.0. We then performed down sample analysis among samples sequenced according to the mapped barcoded reads per cell of each sample and lastly achieved the aggregated matrix. Cells that contained more than 500 expressed genes and mitochondria UMI rate below 40% passed cell quality filtering and mitochondria genes were removed in the expression table.

Seurat package (version: 3.1.0, https://satijalab.org/seurat/) was used for cell normalization and regression based on the expression table according to the UMI counts of each sample and percent of mitochondria rate to obtain the scaled data. PCA was constructed on the basis of the scaled data with top 2000 high variable genes and top 10 principals were used for tSNE construction. Using graph-based cluster method, we acquired the unsupervised cell cluster result based the PCA top 10 principals, and we calculated the marker genes by FindAllMarkers function with Wilcoxon rank sum test algorithm under following criteria:1. lnFC >0.25; 2. P value < 0.05; 3. min.pct > 0.1. To identify the cell type detailed, the clusters of same cell type were selected for re-tSNE analysis, graph-based clustering, and marker analysis.

GO analysis

GO analysis was performed to facilitate elucidating the biological implications of marker genes and differentially expressed genes (*86*). GO annotations from NCBI (www.ncbi.nlm.nih.gov/), UniProt (www.uniprot.org/), and the Gene Ontology (www.geneontology.org/) were downloaded. Fisher's exact tests were applied to identify the significant GO categories, and false discovery rate was used to

correct the *P* values. GO enrichment analysis and comparisons were conducted between: astrocytes of subcluster 9 and astrocytes in other subclusters, $Dmp1^+$ astrocytes and $Dmp1^-$ astrocytes. After excluding *Dmp1*-expressing cells, GO analysis was performed to compare the cell populations between the following: Dendra2-containing endothelial cells in 1M $Dmp1^{Cre}$-$Cox8^{Dendar2}$ mouse brains and endothelial cells in 1M WT mouse brain, and endothelial cell populations of $Dmp1^{Cre}$-$Mfn2^{fl/fl}$ and age-matched WT mouse brains.

GSEA method

GSEA was performed using normalized expression to identify the most significant pathways following Kyoto Encyclopedia of Genes and Genomes (KEGG) gene sets (*87*).

ssGSEA method

The ssGSEA function of GSVA package was used to quantify the enrichment scores of the geneset for each sample cells (*88*).

Bulk RNA sequencing and analysis

For the bulk RNA sequencing (RNA-seq), the total RNA of normal bEnd.3 cell samples (Ctrl, $n = 3$, approximately 100,000 bEnd.3 cells per sample) and bEnd.3 cell samples transplanted with approximately 85 μg of mitochondria (Mito-T, $n = 3$, approximately 100,000 bEnd.3 cells per sample) isolated from primary WT astrocytes was isolated using the RNAmini kit (Qiagen, Germany). RNA quality was examined by gel electrophoresis and with Qubit (Thermo Fisher Scientific, Waltham, MA, USA). Strand-specific libraries were constructed using the TruSeq RNA sample preparation kit (Illumina, San Diego, CA, USA), and sequencing was carried out using the Illumina NovaSeq 6000 instrument by the commercial service of Genergy Biotechnology Co. Ltd. (Shanghai, China). The raw data were handled by Skewer, and data quality was checked by FastQC v0.11.2 (www.bioinformatics.babraham.ac.uk/projects/fastqc/). The read length was 2 × 150 bp. Clean reads were aligned to the Mouse genome mm10 using STAR(2.5.3A), and StringTie software (V1.3.1C) was used for transcript assembly. The expression of the transcript was calculated by FPKM (fragments per kilobase of exon model per million mapped reads) using Perl. Differentially expression transcripts (DETs) were determined using the MA-plot–based method with random sampling (MARS) model in the DEGseq package between different groups (Mito-T versus Ctrl). In general, in MARS model, $M = \log_2C1 - \log_2C2$, and $A = (\log_2C1 + \log_2C2)/2$ (C1 and C2 denote the counts of reads mapped to a specific gene obtained from two samples). The thresholds for determining DETs are $P < 0.05$ and absolute fold change ≥2. Then DETs were chosen for function and signaling pathway enrichment analysis using GO and KEGG databases. The significantly enriched pathways were determined when $P < 0.05$ and at least two affiliated genes were included.

Mitochondrial respiratory complex inhibition

A combination treatment comprising antimycin A (Sigma-Aldrich) and rotenone (Sigma-Aldrich) was used to inhibit mitochondrial complex III and I, respectively, in bEnd.3 endothelial cells. The concentrations of antimycin A/rotenone (A/R) used for dosage sensitivity experiments on bEnd.3 cells in FBS free medium were 0/0, 0.5/0.5, 1/1, 2/2, 4/4, 8/8, and 16/16 μM. After 3 hours of A/R exposure, media was removed, and cells were washed by PBS, followed by a subsequent 24-hour normal incubation in a complete culture medium until further analysis.

Coculture systems

For 2D cocultures, bEnd.3 cells were first plated on 8-mm glass coverslips (ProSciTech) of 24-well plates on day 1 at 50% confluence, and primary astrocytes$^{Mito\text{-}Dendra2}$ were then plated on day 2 for the following 24-hour coculture. Cells were washed and fixed for further staining and imaging. In 3D coculture system for confocal imaging, bEnd.3 cells were cultured on the glass coverslips of 24-well plate, while astrocytes$^{Mito\text{-}Dendra2}$ were separately plated on the upper membrane of the 3-μm-pore Transwell overnight. After washing with PBS separately to remove cell debris, the Transwell plated with astrocytes$^{Mito\text{-}Dendra2}$ was inserted into the well of bEnd.3 cells followed by a 24-hour coculture with bEnd.3 endothelial cells. The bEnd.3 cells on glass coverslips and astrocytes$^{Mito\text{-}Dendra2}$ on Transwell membrane were washed and fixed for further staining and confocal imaging.

For studies of 3D cocultures for flow cytometry analysis, bEnd.3 cells were plated on the bottom of 12-well plates, while primary astrocytes$^{Mito\text{-}Dendra2}$ or $Mfn2^{het}$-astrocytes$^{Mito\text{-}Dendra2}$ were separately plated onto wells of 3-μm-pore Transwell membranes (Biofil). On the second day of culture, bEnd.3 endothelial cells were treated with A/R solution for 3 hours, where relevant. After A/R treatment, Transwells plated with primary astrocytes$^{Mito\text{-}Dendra2}$ or $Mfn2^{het}$-astrocytes$^{Mito\text{-}Dendra2}$ were transferred to dishes for coculturing with bEnd.3 cells. After 24 hours of 3D coculture at 37°C with 5% CO_2, bEnd.3 cells at the bottom of 12-well plates were collected for flow cytometry analysis.

For the experiment of NAC induction on bEnd.3 cells and the following 3D cocultures for flow cytometry analysis, the 2/2 μM A/R-damaged bEnd.3 cells were pretreated with vehicle, 1, 3, 5, and 10 mM NAC (Sigma-Aldrich) for 24 hours before the direct flow cytometry analysis or coculturing with astrocytes$^{Mito\text{-}Dendra2}$ for another 24 hours. For the experiment of H_2O_2 induction assay, astrocytes$^{Mito\text{-}Dendra2}$ were treated with 500 μM H_2O_2 (Sigma-Aldrich) for 4 hours followed by 24 hours of normal culturing before the subsequent 24 hours of 3D coculture with normal bEnd.3 cells or 2/2 μM A/R-damaged bEnd.3 cells before flow cytometry analysis. For the experiment of DMP1 induction assay, astrocytes$^{Mito\text{-}Dendra2}$ were treated with recombinant mouse DMP1 protein (R&D Systems) at the concentrations of 0 ng/ml (vehicle), 50 ng/ml, 100 ng/ml, 200 mg/ml, and 400 ng/ml, respectively, for 24 hours before the subsequent protein extraction or 24 hours of 3D coculture with normal bEnd.3 cells and flow cytometry analysis.

Mitochondrial isolation and transplantation

Mitochondria from primary WT astrocytes or astrocytes$^{Mito\text{-}Dendra2}$ were isolated using the Mitochondrial Isolation Kit for cultured cells (Thermo Fisher Scientific) according to the manufacturer's instructions. For imaging studies of mitochondria isolated from astrocytes$^{Mito\text{-}Dendra2}$, isolated mitochondria were suspended in 100 μl of 200 nM MTR CMXRos (Invitrogen) solution incubated at 37°C for 30 min. Next, 10 μl of mitochondrial suspension was dropped onto a 35-mm glass-bottom petri dish and gently covered with an 8-mm glass coverslip, and this was followed by immediate confocal imaging under a 20× objective of Olympus confocal microscope. For mitochondrial transplantation assays, mitochondria isolated from the donor cells-primary WT astrocytes or astrocytes$^{Mito\text{-}Dendra2}$ were directly coincubated with bEnd.3 cells for 24 hours at 37°C and 5% CO_2. On the basis of the BCA protein assay, quantities of transplanted mitochondria were measured according to the protein

concentration (approximately 850 μg/ml) of 100-μl mitochondrial suspension isolated from 1,000,000 astrocytes. The number of transplanted mitochondria in different experiments is described as the protein weight (micrograms) of isolated mitochondria according to the number of the donor astrocytes.

Evans Blue dye assay

Mice were injected with 2% Evans Blue dye (Sigma-Aldrich) in saline solution intraperitoneally at a concentration of 10 μl/g of body weight for 12 hours. For the assessment of Evans Blue dye leakage, mice were perfused by saline and 4% paraformaldehyde (PFA) intracardially before tissue analysis. For the imaging of blood vessel density and morphology, mice were euthanized by cervical dislocation without perfusion. Mouse brain tissues were collected, processed, and sectioned with a cryostat microtome (Leica). BBB leakage was evaluated by visualizing Evans Blue–stained areas after perfusion, under magnification with a 20× objective of a ZEISS LSM 710 confocal microscope. Blood vessel morphology was assessed by visualizing Evans Blue–filled capillaries without perfusion under a 60× oil immersion objective of Nikon A1 confocal microscope.

For the TCA assay and fluorescence quantification of Evans Blue dye leakage, mice were perfused by saline intracardially to remove the circulating dye in blood before thalamus tissue collection following the published method (*89*). For dye extraction, the thalamus tissues were weighted and placed in 1:4 weight (mg): volume (ml) ratios of 50% TCA, and they were homogenized for 5 min (continuous beating) using a metal-bead homogenizer. The TCA/extracts from the brain samples were centrifuged at 10,000*g* for 20 min to remove precipitates, tissue debris, and metal beads. The supernatants were added to a 96-well plate (30 ml per well), each well supplemented with 90 ml of 95% ethanol and thoroughly mixed for the following high-throughput fluorescence spectroscopy at 620 nm/680 nm.

Cryostat sections

Collected brain tissues were fixed in 4% PFA for 24 hours, followed by storage in PBS at 4°C. Fixed brains were processed for sagittal sectioning, and the right half of brain tissues were gradually dehydrated in 15% sucrose for 24 hours and 30% sucrose for 24 hours. Dehydrated brain tissues were then embedded and frozen in optimal cutting temperature (OCT) medium before sectioning at 20-μm thickness using a cryostat microtome (Leica). The sections were washed and stored in the dark at −20°C until use.

Immunofluorescence

For the immunostaining of fixed cell models, cells that were grown on 8-mm glass coverslips (ProSciTech), or astrocytes grown on 3-μm-pore Transwell membranes were fixed by 4% PFA for 10 min followed with 5-min permeabilization of 0.1 Triton X-100. Cells were then blocked with 3% BSA/PBS for 60 min at room temperature to avoid nonspecific antibody binding and incubated with AQP4 antibody (1:500; Cell Signaling Technology) and CD31 antibody (1:100; R&D Systems) in 0.2% BSA/PBS overnight at room temperature. Cells on coverslip or Transwell membrane were then washed by PBS three times and incubated with donkey anti-goat IgG (H + L) cross-adsorbed secondary antibody, Alexa Fluor 568 (1:200, Thermo Fisher Scientific) and donkey anti-rabbit IgG (H + L) highly cross-adsorbed secondary antibody, Alexa Fluor 647 (1:200, Thermo Fisher Scientific) for 2 hours at room temperature. After washing with PBS three times and incubating with 4′,6-diamidino-2-phenylindole (DAPI) (1:5000) for 10 min at room temperature, the samples were then mounted by mounting medium (Invitrogen). bEnd.3 cells transplanted with free mitochondria labeled by Dendra2 were stained with Alexa Fluor 647 phalloidin (1:500; Invitrogen) for 30 min and DAPI (1:5000) for 10 min at room temperature after fixed with 4% PFA as previously described.

For live cell imaging of 2D cocultured astrocytes$^{Mito\text{-}Dendra2}$ and bEnd3 cells, adherent bEnd3 cells plated on 35-mm glass-bottom confocal dish (P35g-1.5-14-C, MatTek) were previously stained with 100 nM MTR CMXRos (Invitrogen) solution incubated at 37°C for 30 min. After washing with PBS three times, astrocytes$^{Mito\text{-}Dendra2}$ were next plated on the confocal dish to coculture with bEnd.3 endothelial cells overnight before capturing live-cell images. Live-cell images were acquired on Olympus SpinSR microscope using a 60× oil immersion objective in a temperature-controlled chamber (37°C, 5% CO_2).

For the immunostaining of S100β, AQP4, or CD31 on *Dmp1*^{Cre}-*Ai9*, *Dmp1*^{Cre}-*mGmT*, *Dmp1*^{Cre}-*Cox8*^{Dendra2}, and *Dmp1*^{Cre}-*Cox8*^{Dendra2}-*Mfn2*$^{fl/fl}$ mouse brain sections, mice were perfused by saline and 4% PFA intracardially before tissue collection. For the immunostaining of COL4A1 on *Dmp1*^{Cre}-*Mfn2*$^{fl/fl}$ mouse brains, mice were euthanized by cervical dislocation without perfusion and brain tissues were collected freshly for further processing. Cryostat brain sections were fixed by 4% PFA for 10 min, washed with PBS three times, permeabilized in 0.1% Triton X-100/PBS for 10 min, washed with PBS three times, and then blocked with 3% BSA/PBS for 60 min at room temperature to avoid nonspecific antibody binding. Brian sections were then incubated with S100β antibody (1:100; Abcam), AQP4 antibody (1:500; Cell Signaling Technology) (1:50, Santa Cruz Biotechnology), CD31 antibody (1:100; R&D Systems) (1:100; Dako), and COL4A1 antibody (1:100; Novus Biologicals) in 0.2% BSA/PBS overnight at room temperature. Sections were then washed by PBS three times and incubated with corresponding donkey anti-rabbit IgG (H + L) highly cross-adsorbed secondary antibody, Alexa Fluor 488 (1:200, Thermo Fisher Scientific), donkey anti-rabbit IgG (H + L) highly cross-adsorbed secondary antibody, Alexa Fluor 568 (1:200, Thermo Fisher Scientific), donkey anti-rabbit IgG (H + L) highly cross-adsorbed secondary antibody, Alexa Fluor 647 (1:200, Thermo Fisher Scientific), donkey anti-goat IgG (H + L) cross-adsorbed secondary antibody, Alexa Fluor 568 (1:200, Thermo Fisher Scientific), donkey anti-goat IgG (H + L) cross-adsorbed secondary antibody, Alexa Fluor 647 (1:200, Thermo Fisher Scientific), donkey anti-mouse IgG (H + L) cross-adsorbed secondary antibody, Alexa Fluor 568 (1:200, Thermo Fisher Scientific), donkey anti-mouse IgG (H + L) cross-adsorbed secondary antibody, Alexa Fluor 647 (1:200, Thermo Fisher Scientific) for 2 hours at room temperature in corresponding experiments. Sections were then washed by PBS three times and incubated with DAPI (1:5000) for 10 min at room temperature. After washing with PBS three times, brain sections were mounted under glass coverslips using ProLong Diamond antifade medium (Invitrogen) and dried overnight before confocal imaging.

Confocal imaging and analysis

Live-cell images were acquired on Olympus SpinSR microscope using a 60× oil immersion objective in a temperature-controlled chamber (37°C, 5% CO_2). Images of fixed cells or brain sections were obtained on ZEISS LSM 710, downward Leica SP8 and Nikon

A1 confocal microscope by serial scanning along the Z-axis. Images were acquired using ZEISS ZEN microscope software, Leica LAS X software, or Fiji Image J software (NIH). 2D cocultured bEnd.3 cells and astrocytes were imaged by 63× oil immersion objective of Leica SP8 confocal microscope. For imaging of astrocytes on Transwell membranes in 3D coculture system after proper fixation and staining, the membranes were cut and mounted with ProLong Diamond antifade medium (Invitrogen) and then covered with glass coverslips. Mounted bEnd.3 cells on glass coverslips and astrocytes on Transwell membranes were imaged under 63× oil immersion objective of ZEISS LSM 710 confocal microscope. bEnd.3 cells transplanted with mitochondria were imaged by ZEISS LSM 710 confocal microscope under 20× objectives after proper fixation and immunostaining. Sagittal map of tdTomato signals in *Dmp1*^{Cre}-*mGmT* mouse brain sections were obtained under Leica SP8 confocal microscope by large image scanning with 5% overlap. Sagittal map of Dendra2 signals in *Dmp1*^{Cre}-*Cox8*^{Dendra2} mouse brain sections were obtained under Nikon A1 confocal microscope by large image scanning with 10% overlap. Immunostaining of CD31 and AQP4 on *Dmp1*^{Cre}-*mGmT* mouse brain sections was imaged by Leica SP8 confocal microscope. Immunostaining of CD31 and AQP4 on *Dmp1*^{Cre}-*Cox8*^{Dendra2} mouse brain sections and COL4A1 on *Dmp1*^{Cre}-*Mfn2*$^{fl/fl}$ mouse brain sections were imaged by Nikon A1 microscope.

TEM imaging

Anesthetized mice were transcardially perfused with saline solution, followed by the perfusion of fixative solution containing 4% PFA and 0.25% glutaraldehyde (1:1) in PBS. The brain tissues were isolated and cut into 1-mm-thick sagittal sections and small portions of the thalamus were dissected. The dissected thalamus tissues were then fixed in the fixative solution containing 4% PFA and 0.25% glutaraldehyde (1:1) in PBS at 4°C for 3 hours before further processing. Fixed tissues were then rinsed by 0.1 M phosphate buffer (pH 7.2) three times and postfixed in 1% OsO4 in the same buffer at 4°C for 3 hours. After being rinsed three times, tissues were then dehydrated in a graded ethanol series and embedded in Epon812 resin. For electron microscopy, ultrathin sections of 70 nm thick were cut from tissue resin blocks. The sections were then picked up on formvar-coated copper mesh grids and doubly stained with saturated uranyl acetate for 30 min followed by lead citrate for 15 min. Ultrathin sections on the grids were examined in a Thermo Fisher Scientific Talos 120 transmission electron microscope at 120 kV and images of capillary lumens surrounded by astrocytic endfeet were captured. The distance from the outer membrane of mitochondria in astrocytic endfeet to the capillary lumens was determined in Photoshop software following a manual drawing of single organelles. All parameters obtained from one field of view were averaged together.

Flow cytometry analysis

To detect mitochondrial ROS level and mitochondrial transfer efficiency, bEnd.3 cells treated with/without A/R, bEnd.3 cells treated with/without NAC were cultured either alone or cocultured with primary astrocytes$^{\text{Mito-Dendra2}}$, *Mfn2*^{het}-astrocytes$^{\text{Mito-Dendra2}}$, DMP1-treated astrocytes$^{\text{Mito-Dendra2}}$ or H_2O_2-treated astrocytes$^{\text{Mito-Dendra2}}$. Before cell collection, bEnd.3 cells were stained with 5 μM MitoSOX (Invitrogen) for 10 min at 37°C. For the assessment of the alleviation of ROS accumulation after mitochondrial transplantation, 2/2 μM A/R-treated bEnd.3 endothelial cells were coincubated with mitochondria isolated from primary WT astrocytes in 12-well plates and stained with 10 μM H_2DCFDA (Solarbio) for 20 min at 37°C. After the staining was completed, cells were washed, digested and resuspended in 2% FBS/PBS medium for flow cytometry analysis by CytoFlex (Beckman Coulter). Fluorescence intensity of Dendra2, MitoSOX, or H_2DCFDA in bEnd.3 cells were further analyzed by Flowjo software.

Flow cytometry analysis on *Dmp1*^{Cre}-*Cox8*^{Dendra2} mouse brains were performed for further assessing the numbers of endothelial cells incorporating astrocytes^{Dmp1}-originated mitochondria among all brain endothelial cells. In detail, the whole brain tissues from 4 Dmp1$^{\text{Cre}}$-Cox8$^{\text{Dendra2}}$ mice were digested to make single cell suspensions according to the protocol of performing scRNA-seq. Cell suspensions were stained by APC anti-mouse CD31 antibody (Biolegend) and were then resuspended in PBS containing 2% FBS for immediate flow cytometry analysis. The cell percentage of Dendra2^{+}CD31^{+} cells were quantified among all CD31^{+} cells.

Western blotting

Proteins from cells or dissected thalamus tissue from the hemisphere of mouse brains were extracted by incubating in cell lysis reagent (Sigma-Aldrich) containing a cocktail of protease inhibitor, phosphatase inhibitor, and EDTA for 20 min at 4°C, followed by centrifugation at 14,000*g* for 20 min at 4°C. Protein concentrations were determined using BCA protein assay kit. Protein suspensions were then diluted in 5× SDS loading buffer and boiled for 5 min at 95°C. For each sample, defined amounts of protein suspension were fractionated in 4 to 20% SDS-PAGE Gel and transferred to PVDF membrane (Millipore). Membranes were then incubated with primary antibodies, including Beta-Actin antibody (1:5000, Cell Signaling Technology), Mfn2 antibody (1:1000, Cell Signaling Technology), P53 antibody (1:1000; Cell Signaling Technology), P19 antibody (1:1000; Abcam) at 4°C overnight, followed by incubation with corresponding HRP-linked anti-mouse secondary antibodies (1:5000; Cell Signaling Technology) and HRP-linked anti-rabbit secondary antibodies (1:5000, Cell Signaling Technology). Proteins were visualized by enhanced chemiluminescence and autoradiography (ChemiDoc MP Imaging Systems, Bio-Rad).

RNA isolation and real-time qPCR

For isolating RNA from primary astrocytes, RNA was isolated from the PBS-washed adhering cells using the RNA purification kit (EZ-bioscience) according to the manufacturer's protocol. RNA concentration was assessed with Nanodrop spectrophotometers (Thermo Fisher Scientific). For reverse transcription, 500 ng RNA was reverse transcribed using 4 × Reverse Transcription Master Mix (EZbioscience). qPCR was performed using 2 × SYBR Green Color qPCR Mix (EZbioscience) following the manufacturer's recommendation. Samples were tested on a QuantStudio 7 Flex Real-Time PCR System (Thermo Fisher Scientific). The results were calculated using the ΔΔCT method and are presented as fold increase relative to *Gapdh* mRNA levels. Primers of *Gapdh*, *Mfn2*, *Ki67*, *mt-Atp6*, and *Pgc-1 alpha* are listed in table S1.

CCK-8 cell viability assay

The viability of primary WT astrocytes or *Mfn2*^{het}-astrocytes was assessed by CCK-8 assay (Meilunbio). Astrocytes of passage 3 were seeded on 96-well plates at 8000 cells per well. After 36 hours of cell

culture, 10% CCK-8 solution was added to each well for 3 hours according to the instrument, and the absorbance value was then measured at 459 nm by using a Multiscan Spectrum (Bio-Rad).

Trypan blue dye uptake assay

Trypan Blue (~900 Da) was used to assess the membrane integrity of cells according to the reported instruction (*90*). 0.08% Trypan Blue dyes were added into bEnd.3 cells immediately after the treatment of 3-hour 2 μM A/R, 3-hour vehicle solution, or 5-min 0.1% Triton X-100 (positive control). After staining for 5 min, the dyes were subsequently removed and washed with PBS three times, and the proportion of dye-positive cells was assessed by Nikon NIS microscopy.

Cell scratch and wound healing assay

bEnd.3 endothelial cells were cultured in 12-well plates to a confluency of 90% (approximately 200,000 cells), and then two-thirds of the samples were exposured to A/R. Half of the A/R-damaged bEnd.3 cell samples were then coincubated with approximately 170 μg of astrocytes-derived mitochondria. After 24 hours of further coincubation to enable cell confluency reach to almost 100%, a cell-culture wound model was established by scratching with sterile pipette tips. After the removal of floating cells, these initial cellular wounds were immediately documented using a Nikon microscope. The wounds were then allowed to heal for 24 hours in FBS-free medium and photographed using a Nikon microscope. The wound healing rate was measured as the ratio of wound area recovered by cells to the initially devoid of cellular cover.

Statistical analysis

Statistical analysis was performed by GraphPad Prism software (version 9). The quantification of confocal images and Western blot images was conducted by a blinded observer of the experimental conditions. For the comparison of the mean values between two groups, two-tailed Student's paired or unpaired *t* test was used as claimed in corresponding quantification results. Multigroup individual datasets with normal distribution were compared using one-way analysis of variance (ANOVA) with Tukey's post hoc test. Data are presented as the means ± SEM. For the relevant statistical analysis of scRNA-seq data, Wilcoxon rank sum test was used and data are presented as median (interquartile range). The exact number of replicates is given in each figure legend. Significance in all figures is denoted as follows: $*P < 0.05$, $**P < 0.01$, $***P < 0.001$, $****P < 0.0001$.

Supplementary Materials

This PDF file includes:

Figs. S1 to S13
Table S1

REFERENCES AND NOTES

1. R. Daneman, A. Prat, The blood-brain barrier. *Cold Spring Harb. Perspect. Biol.* **7**, a020412 (2015).
2. D. J. Begley, M. W. Brightman, Structural and functional aspects of the blood-brain barrier. *Prog. Drug Res.* **61**, 39–78 (2003).
3. N. J. Abbott, Evidence for bulk flow of brain interstitial fluid: Significance for physiology and pathology. *Neurochem. Int.* **45**, 545–552 (2004).
4. N. J. Abbott, Dynamics of CNS barriers: Evolution, differentiation, and modulation. *Cell. Mol. Neurobiol.* **25**, 5–23 (2005).
5. N. J. Abbott, L. Rönnbäck, E. Hansson, Astrocyte–endothelial interactions at the blood–brain barrier. *Nat. Rev. Neurosci.* **7**, 41–53 (2006).
6. F. Erdo, L. Denes, E. de Lange, Age-associated physiological and pathological changes at the blood-brain barrier: A review. *J. Cereb. Blood Flow Metab.* **37**, 4–24 (2017).
7. Y. Pan, J. A. Nicolazzo, Impact of aging, Alzheimer's disease and Parkinson's disease on the blood-brain barrier transport of therapeutics. *Adv. Drug Deliv. Rev.* **135**, 62–74 (2018).
8. E. A. van Vliet, X. E. Ndode-Ekane, L. J. Lehto, J. A. Gorter, P. Andrade, E. Aronica, O. Grohn, A. Pitkanen, Long-lasting blood-brain barrier dysfunction and neuroinflammation after traumatic brain injury. *Neurobiol. Dis.* **145**, 105080 (2020).
9. S. Sulhan, K. A. Lyon, L. A. Shapiro, J. H. Huang, Neuroinflammation and blood-brain barrier disruption following traumatic brain injury: Pathophysiology and potential therapeutic targets. *J. Neurosci. Res.* **98**, 19–28 (2020).
10. D. Shlosberg, M. Benifla, D. Kaufer, A. Friedman, Blood-brain barrier breakdown as a therapeutic target in traumatic brain injury. *Nat. Rev. Neurol.* **6**, 393–403 (2010).
11. W. Zhang, L. Zhu, C. An, R. Wang, L. Yang, W. Yu, P. Li, Y. Gao, The blood brain barrier in cerebral ischemic injury–Disruption and repair. *Brain Hemorrhages* **1**, 34–53 (2020).
12. Y. Zhang, B. A. Barres, Astrocyte heterogeneity: An underappreciated topic in neurobiology. *Curr. Opin. Neurobiol.* **20**, 588–594 (2010).
13. I. Matias, J. Morgado, F. C. A. Gomes, Astrocyte heterogeneity: Impact to brain aging and disease. *Front. Aging Neurosci.* **11**, 59 (2019).
14. M. Y. Batiuk, A. Martirosyan, J. Wahis, F. de Vin, C. Marneffe, C. Kusserow, J. Koeppen, J. F. Viana, J. F. Oliveira, T. Voet, C. P. Ponting, T. G. Belgard, M. G. Holt, Identification of region-specific astrocyte subtypes at single cell resolution. *Nat. Commun.* **11**, 1220 (2020).
15. M. R. Freeman, D. H. Rowitch, Evolving concepts of gliogenesis: A look way back and ahead to the next 25 years. *Neuron* **80**, 613–623 (2013).
16. N. J. Abbott, Blood-brain barrier structure and function and the challenges for CNS drug delivery. *J. Inherit. Metab. Dis.* **36**, 437–449 (2013).
17. S. W. Lee, W. J. Kim, Y. K. Choi, H. S. Song, M. J. Son, I. H. Gelman, Y. J. Kim, K. W. Kim, SSeCKS regulates angiogenesis and tight junction formation in blood-brain barrier. *Nat. Med.* **9**, 900–906 (2003).
18. J. Gbel, E. Engelhardt, P. Pelzer, V. Sakthivelu, H. M. Jahn, M. Jevtic, K. Folz-Donahue, C. Kukat, A. Schauss, C. K. Frese, P. Giavalisco, A. Ghanem, K. K. Conzelmann, E. Motori, M. Bergami, Mitochondria-endoplasmic reticulum contacts in reactive astrocytes promote vascular remodeling. *Cell Metab.* **31**, 791–808.e8 (2020).
19. M. N. Islam, S. R. Das, M. T. Emin, M. Wei, L. Sun, K. Westphalen, D. J. Rowlands, S. K. Quadri, S. Bhattacharya, J. Bhattacharya, Mitochondrial transfer from bone-marrow-derived stromal cells to pulmonary alveoli protects against acute lung injury. *Nat. Med.* **18**, 759–765 (2012).
20. T. Ahmad, S. Mukherjee, B. Pattnaik, M. Kumar, S. Singh, M. Kumar, R. Rehman, B. K. Tiwari, K. A. Jha, A. P. Barhanpurkar, M. R. Wani, S. S. Roy, U. Mabalirajan, B. Ghosh, A. Agrawal, Miro1 regulates intercellular mitochondrial transport & enhances mesenchymal stem cell rescue efficacy. *EMBO J.* **33**, 994–1010 (2014).
21. D. Liu, Y. Gao, J. Liu, Y. Huang, J. Yin, Y. Feng, L. Shi, B. P. Meloni, C. Zhang, M. Zheng, J. Gao, Intercellular mitochondrial transfer as a means of tissue revitalization. *Signal Transduct. Target. Ther.* **6**, 65 (2021).
22. W. H. Oldendorf, M. E. Cornford, W. J. Brown, The large apparent work capability of the blood-brain barrier: A study of the mitochondrial content of capillary endothelial cells in brain and other tissues of the rat. *Ann. Neurol.* **1**, 409–417 (1977).
23. D. N. Doll, H. Hu, J. Sun, S. E. Lewis, J. W. Simpkins, X. Ren, Mitochondrial crisis in cerebrovascular endothelial cells opens the blood-brain barrier. *Stroke* **46**, 1681–1689 (2015).
24. M. J. Lee, Y. Jang, J. Han, S. J. Kim, X. Ju, Y. L. Lee, J. Cui, J. Zhu, M. J. Ryu, S. Y. Choi, W. Chung, C. Heo, H. S. Yi, H. J. Kim, Y. H. Huh, S. K. Chung, M. Shong, G. R. Kweon, J. Y. Heo, Endothelial-specific Crif1 deletion induces BBB maturation and disruption via the alteration of actin dynamics by impaired mitochondrial respiration. *J. Cereb. Blood Flow Metab.* **40**, 1546–1561 (2020).
25. L. Cheslow, J. I. Alvarez, Glial-endothelial crosstalk regulates blood-brain barrier function. *Curr. Opin. Pharmacol.* **26**, 39–46 (2016).
26. C. F. Lien, S. K. Mohanta, M. Frontczak-Baniewicz, J. D. Swinny, B. Zablocka, D. C. Gorecki, Absence of glial α-dystrobrevin causes abnormalities of the blood-brain barrier and progressive brain edema. *J. Biol. Chem.* **287**, 41374–41385 (2012).
27. H. Wolburg, S. Noell, K. Wolburg-Buchholz, A. Mack, P. Fallier-Becker, Agrin, aquaporin-4, and astrocyte polarity as an important feature of the blood-brain barrier. *Neuroscientist* **15**, 180–193 (2009).
28. Y. He, Y. Yao, S. E. Tsirka, Y. Cao, Cell-culture models of the blood–brain barrier. *Stroke* **45**, 2514–2526 (2014).
29. C. Lehner, R. Gehwolf, H. Tempfer, I. Krizbai, B. Hennig, H. C. Bauer, H. Bauer, Oxidative stress and blood-brain barrier dysfunction under particular consideration of matrix metalloproteinases. *Antioxid. Redox Signal.* **15**, 1305–1323 (2011).
30. J. J. Lochhead, G. McCaffrey, C. E. Quigley, J. Finch, K. M. DeMarco, N. Nametz, T. P. Davis, Oxidative stress increases blood-brain barrier permeability and induces alterations in occludin during hypoxia-reoxygenation. *J. Cereb. Blood Flow Metab.* **30**, 1625–1636 (2010).

31. P. B. Pun, J. Lu, S. Moochhala, Involvement of ROS in BBB dysfunction. *Free Radic. Res.* **43**, 348–364 (2009).
32. C. R. Marlein, L. Zaitseva, R. E. Piddock, S. D. Robinson, D. R. Edwards, M. S. Shafat, Z. Zhou, M. Lawes, K. M. Bowles, S. A. Rushworth, NADPH oxidase-2 derived superoxide drives mitochondrial transfer from bone marrow stromal cells to leukemic blasts. *Blood* **130**, 1649–1660 (2017).
33. J. J. Mistry, C. R. Marlein, J. A. Moore, C. Hellmich, E. E. Wojtowicz, J. G. W. Smith, I. Macaulay, Y. Sun, A. Morfakis, A. Patterson, R. H. Horton, D. Divekar, C. J. Morris, A. Haestier, F. Di Palma, N. Beraza, K. M. Bowles, S. A. Rushworth, ROS-mediated PI3K activation drives mitochondrial transfer from stromal cells to hematopoietic stem cells in response to infection. *Proc. Natl. Acad. Sci. U.S.A.* **116**, 24610–24619 (2019).
34. B. E. Clarke, D. M. Taha, G. E. Tyzack, R. Patani, Regionally encoded functional heterogeneity of astrocytes in health and disease: A perspective. *Glia* **69**, 20–27 (2021).
35. M. Amiry-Moghaddam, T. Otsuka, P. D. Hurn, R. J. Traystman, F. M. Haug, S. C. Froehner, M. E. Adams, J. D. Neely, P. Agre, O. P. Ottersen, A. Bhardwaj, An alpha-syntrophin-dependent pool of AQP4 in astroglial end-feet confers bidirectional water flow between blood and brain. *Proc. Natl. Acad. Sci. U.S.A.* **100**, 2106–2111 (2003).
36. K. Wolburg-Buchholz, A. F. Mack, E. Steiner, F. Pfeiffer, B. Engelhardt, H. Wolburg, Loss of astrocyte polarity marks blood-brain barrier impairment during experimental autoimmune encephalomyelitis. *Acta Neuropathol.* **118**, 219–233 (2009).
37. L. W. Fisher, A. Jain, M. Tayback, N. S. Fedarko, Small integrin binding ligand N-linked glycoprotein gene family expression in different cancers. *Clin. Cancer Res.* **10**, 8501–8511 (2004).
38. A. Bellahcene, V. Castronovo, K. U. Ogbureke, L. W. Fisher, N. S. Fedarko, Small integrin-binding ligand N-linked glycoproteins (SIBLINGs): Multifunctional proteins in cancer. *Nat. Rev. Cancer* **8**, 212–226 (2008).
39. B. Jing, C. Zhang, X. Liu, L. Zhou, J. Liu, Y. Yao, J. Yu, Y. Weng, M. Pan, J. Liu, Z. Wang, Y. Sun, Y. E. Sun, Glycosylation of dentin matrix protein 1 is a novel key element for astrocyte maturation and BBB integrity. *Protein Cell* **9**, 298–309 (2018).
40. B. Xiong, A. Li, Y. Lou, S. Chen, B. Long, J. Peng, Z. Yang, T. Xu, X. Yang, X. Li, T. Jiang, Q. Luo, H. Gong, Precise cerebral vascular atlas in stereotaxic coordinates of whole mouse brain. *Front. Neuroanat.* **11**, 128 (2017).
41. J. Gao, A. Qin, D. Liu, R. Ruan, Q. Wang, J. Yuan, T. S. Cheng, A. Filipovska, J. M. Papadimitriou, K. Dai, Q. Jiang, X. Gao, J. Q. Feng, H. Takayanagi, C. Zhang, M. H. Zheng, Endoplasmic reticulum mediates mitochondrial transfer within the osteocyte dendritic network. *Sci. Adv.* **5**, eaaw7215 (2019).
42. S. M. Davidson, M. R. Duchen, Endothelial mitochondria: Contributing to vascular function and disease. *Circ. Res.* **100**, 1128–1141 (2007).
43. C. Greene, N. Hanley, C. R. Reschke, A. Reddy, M. A. Mae, R. Connolly, C. Behan, E. O'Keeffe, I. Bolger, N. Hudson, C. Delaney, M. A. Farrell, D. F. O'Brien, J. Cryan, F. M. Brett, A. Beausang, C. Betsholtz, D. C. Henshall, C. P. Doherty, M. Campbell, Microvascular stabilization via blood-brain barrier regulation prevents seizure activity. *Nat. Commun.* **13**, 2003 (2022).
44. M. S. Thomsen, L. J. Routhe, T. Moos, The vascular basement membrane in the healthy and pathological brain. *J. Cereb. Blood Flow Metab.* **37**, 3300–3317 (2017).
45. A. C. Court, A. Le-Gatt, P. Luz-Crawford, E. Parra, V. Aliaga-Tobar, L. F. Batiz, R. A. Contreras, M. I. Ortuzar, M. Kurte, R. Elizondo-Vega, V. Maracaja-Coutinho, K. Pino-Lagos, F. E. Figueroa, M. Khoury, Mitochondrial transfer from MSCs to T cells induces Treg differentiation and restricts inflammatory response. *EMBO Rep.* **21**, e48052 (2020).
46. L. Lamalice, F. Le Boeuf, J. Huot, Endothelial cell migration during angiogenesis. *Circ. Res.* **100**, 782–794 (2007).
47. B. Obermeier, R. Daneman, R. M. Ransohoff, Development, maintenance and disruption of the blood-brain barrier. *Nat. Med.* **19**, 1584–1596 (2013).
48. H. S. Lee, J. Han, H. J. Bai, K. W. Kim, Brain angiogenesis in developmental and pathological processes: Regulation, molecular and cellular communication at the neurovascular interface. *FEBS J.* **276**, 4622–4635 (2009).
49. C. C. Liang, A. Y. Park, J. L. Guan, In vitro scratch assay: A convenient and inexpensive method for analysis of cell migration in vitro. *Nat. Protoc.* **2**, 329–333 (2007).
50. K. Hayakawa, E. Esposito, X. Wang, Y. Terasaki, Y. Liu, C. Xing, X. Ji, E. H. Lo, Transfer of mitochondria from astrocytes to neurons after stroke. *Nature* **535**, 551–555 (2016).
51. K. English, A. Shepherd, N. E. Uzor, R. Trinh, A. Kavelaars, C. J. Heijnen, Astrocytes rescue neuronal health after cisplatin treatment through mitochondrial transfer. *Acta Neuropathol. Commun.* **8**, 36 (2020).
52. C.-H. Davis, K. Y. Kim, E. A. Bushong, E. A. Mills, D. Boassa, T. Shih, M. Kinebuchi, S. Phan, Y. Zhou, N. A. Bihlmeyer, J. V. Nguyen, Y. Jin, M. H. Ellisman, N. Marsh-Armstrong, Transcellular degradation of axonal mitochondria. *Proc. Natl. Acad. Sci. U.S.A.* **111**, 9633–9638 (2014).
53. P. K. Eide, M. M. Hasan-Olive, H. A. Hansson, R. Enger, Increased occurrence of pathological mitochondria in astrocytic perivascular endfoot processes and neurons of idiopathic intracranial hypertension. *J. Neurosci. Res.* **99**, 467–480 (2021).
54. M. M. Hasan-Olive, H. A. Hansson, R. Enger, E. A. Nagelhus, P. K. Eide, Blood-brain barrier dysfunction in idiopathic intracranial hypertension. *J. Neuropathol. Exp. Neurol.* **78**, 808–818 (2019).
55. R. Filadi, D. Pendin, P. Pizzo, Mitofusin 2: From functions to disease. *Cell Death Dis.* **9**, 330 (2018).
56. A. M. Falchi, V. Sogos, F. Saba, M. Piras, T. Congiu, M. Piludu, Astrocytes shed large membrane vesicles that contain mitochondria, lipid droplets and ATP. *Histochem. Cell Biol.* **139**, 221–231 (2013).
57. J. H. Park, E. H. Lo, K. Hayakawa, Endoplasmic reticulum interaction supports energy production and redox homeostasis in mitochondria released from astrocytes. *Transl. Stroke Res.* **12**, 1045–1054 (2021).
58. S. Murru, S. Hess, E. Barth, E. R. Almajan, D. Schatton, S. Hermans, S. Brodesser, T. Langer, P. Kloppenburg, E. I. Rugarli, Astrocyte-specific deletion of the mitochondrial m-AAA protease reveals glial contribution to neurodegeneration. *Glia* **67**, 1526–1541 (2019).
59. H. G. Lee, M. A. Wheeler, F. J. Quintana, Function and therapeutic value of astrocytes in neurological diseases. *Nat. Rev. Drug Discov.* **21**, 339–358 (2022).
60. B. A. MacVicar, E. A. Newman, Astrocyte regulation of blood flow in the brain. *Cold Spring Harb. Perspect. Biol.* **7**, a020388 (2015).
61. K. Braet, K. Paemeleire, K. D'Herde, M. J. Sanderson, L. Leybaert, Astrocyte–endothelial cell calcium signals conveyed by two signalling pathways. *Eur. J. Neurosci.* **13**, 79–91 (2008).
62. S. H. van Ierssel, V. M. Conraads, E. M. Van Craenenbroeck, Y. Liu, A. I. Maas, P. M. Parizel, V. Y. Hoymans, C. J. Vrints, P. G. Jorens, Endothelial dysfunction in acute brain injury and the development of cerebral ischemia. *J. Neurosci. Res.* **93**, 866–872 (2015).
63. F. Wang, Y. Cao, L. Ma, H. Pei, W. D. Rausch, H. Li, Dysfunction of cerebrovascular endothelial cells: Prelude to vascular dementia. *Front. Aging Neurosci.* **10**, 376 (2018).
64. S. I. Graves, D. J. Baker, Implicating endothelial cell senescence to dysfunction in the ageing and diseased brain. *Basic Clin. Pharmacol. Toxicol.* **127**, 102–110 (2020).
65. J. H. Park, Y. Nakamura, W. Li, G. Hamanaka, K. Arai, E. H. Lo, K. Hayakawa, Effects of O-GlcNAcylation on functional mitochondrial transfer from astrocytes. *J. Cereb. Blood Flow Metab.* **41**, 1523–1535 (2021).
66. D. C. Watson, D. Bayik, S. Storevik, S. S. Moreino, S. A. Sprowls, J. Han, M. T. Augustsson, A. Lauko, P. Sravya, G. V. Røsland, K. Troike, K. J. Tronstad, S. Wang, K. Sarnow, K. Kay, T. R. Lunavat, D. J. Silver, S. Dayal, J. V. Joseph, E. Mulkearns-Hubert, L. A. R. Ystaas, G. Deshpande, J. Guyon, Y. Zhou, C. R. Magaut, J. Seder, L. Neises, S. E. Williford, J. Meiser, A. J. Scott, P. Sajjakulnukit, J. A. Mears, R. Bjerkvig, A. Chakraborty, T. Daubon, F. Cheng, C. A. Lyssiotis, D. R. Wahl, A. B. Hjelmeland, J. A. Hossain, H. Miletic, J. D. Lathia, GAP43-dependent mitochondria transfer from astrocytes enhances glioblastoma tumorigenicity. *Nat. Cancer* **4**, 648–664 (2023).
67. T. Awasaki, S. L. Lai, K. Ito, T. Lee, Organization and postembryonic development of glial cells in the adult central brain of *Drosophila*. *J. Neurosci.* **28**, 13742–13753 (2008).
68. C. Hochstim, B. Deneen, A. Lukaszewicz, Q. Zhou, D. J. Anderson, Identification of positionally distinct astrocyte subtypes whose identities are specified by a homeodomain code. *Cell* **133**, 510–522 (2008).
69. L. Hosli, M. Zuend, G. Bredell, H. S. Zanker, C. E. Porto de Oliveira, A. S. Saab, B. Weber, Direct vascular contact is a hallmark of cerebral astrocytes. *Cell Rep.* **39**, 110599 (2022).
70. J. Q. Feng, J. H. Zhang, S. L. Dallas, Y. B. Lu, S. Chen, X. Y. Tan, M. Owen, S. E. Harris, M. MacDougall, Dentin matrix protein 1, a target molecule for Cbfa1 in bone, is a unique bone marker gene. *J. Bone Miner. Res.* **17**, 1822–1831 (2002).
71. A. George, A. Ramachandran, M. Albazzaz, S. Ravindran, DMP1--a key regulator in mineralized matrix formation. *J. Musculoskelet. Neuronal Interact.* **7**, 308 (2007).
72. J. Q. Feng, L. M. Ward, S. Liu, Y. Lu, Y. Xie, B. Yuan, X. Yu, F. Rauch, S. I. Davis, S. Zhang, H. Rios, M. K. Drezner, L. D. Quarles, L. F. Bonewald, K. E. White, Loss of DMP1 causes rickets and osteomalacia and identifies a role for osteocytes in mineral metabolism. *Nat. Genet.* **38**, 1310–1315 (2006).
73. A. Lafzi, C. Moutinho, S. Picelli, H. Heyn, Tutorial: Guidelines for the experimental design of single-cell RNA sequencing studies. *Nat. Protoc.* **13**, 2742–2757 (2018).
74. C. S. Baron, A. Barve, M. J. Muraro, R. van der Linden, G. Dharmadhikari, A. Lyubimova, E. J. P. de Koning, A. van Oudenaarden, Cell type purification by single-cell transcriptome-trained sorting. *Cell* **179**, 527–542.e19 (2019).
75. M. N. Artyomov, J. Van den Bossche, Immunometabolism in the single-cell era. *Cell Metab.* **32**, 710–725 (2020).
76. E. M. Llufrio, L. Wang, F. J. Naser, G. J. Patti, Sorting cells alters their redox state and cellular metabolome. *Redox Biol.* **16**, 381–387 (2018).
77. H. A. Segeren, K. C. Andree, L. Oomens, B. Westendorp, Collection of cells for single-cell RNA sequencing using high-resolution fluorescence microscopy. *STAR Protoc.* **2**, 100718 (2021).
78. L. Kaplan, B. W. Chow, C. Gu, Neuronal regulation of the blood–brain barrier and neurovascular coupling. *Nat. Rev. Neurosci.* **21**, 416–432 (2020).
79. C. Lopez-Crisosto, C. Pennanen, C. Vasquez-Trincado, P. E. Morales, R. Bravo-Sagua, A. F. G. Quest, M. Chiong, S. Lavandero, Sarcoplasmic reticulum-mitochondria communication in cardiovascular pathophysiology. *Nat. Rev. Cardiol.* **14**, 342–360 (2017).
80. S. Chalmers, C. Saunter, C. Wilson, P. Coats, J. M. Girkin, J. G. McCarron, Mitochondrial motility and vascular smooth muscle proliferation. *Arterioscler. Thromb. Vasc. Biol.* **32**, 3000–3011 (2012).
81. K. Kisler, A. R. Nelson, A. Montagne, B. V. Zlokovic, Cerebral blood flow regulation and neurovascular dysfunction in Alzheimer disease. *Nat. Rev. Neurosci.* **18**, 419–434 (2017).

82. A. Armulik, G. Genove, M. Mae, M. H. Nisancioglu, E. Wallgard, C. Niaudet, L. He, J. Norlin, P. Lindblom, K. Strittmatter, B. R. Johansson, C. Betsholtz, Pericytes regulate the blood-brain barrier. *Nature* **468**, 557–561 (2010).
83. Y. Lu, Y. Xie, S. Zhang, V. Dusevich, L. F. Bonewald, J. Q. Feng, DMP1-targeted Cre expression in odontoblasts and osteocytes. *J. Dent. Res.* **86**, 320–325 (2007).
84. S. Schildge, C. Bohrer, K. Beck, C. Schachtrup, Isolation and culture of mouse cortical astrocytes. *J. Vis. Exp.*, (2013).
85. S. Chen, Y. Zhou, Y. Chen, J. Gu, fastp: An ultra-fast all-in-one FASTQ preprocessor. *Bioinformatics* **34**, i884–i890 (2018).
86. M. Ashburner, C. A. Ball, J. A. Blake, D. Botstein, H. Butler, J. M. Cherry, A. P. Davis, K. Dolinski, S. S. Dwight, J. T. Eppig, M. A. Harris, D. P. Hill, L. Issel-Tarver, A. Kasarskis, S. Lewis, J. C. Matese, J. E. Richardson, M. Ringwald, G. M. Rubin, G. Sherlock, Gene ontology: Tool for the unification of biology. The Gene Ontology Consortium. *Nat. Genet.* **25**, 25–29 (2000).
87. A. Subramanian, P. Tamayo, V. K. Mootha, S. Mukherjee, B. L. Ebert, M. A. Gillette, A. Paulovich, S. L. Pomeroy, T. R. Golub, E. S. Lander, J. P. Mesirov, Gene set enrichment analysis: A knowledge-based approach for interpreting genome-wide expression profiles. *Proc. Natl. Acad. Sci. U.S.A.* **102**, 15545–15550 (2005).
88. D. A. Barbie, P. Tamayo, J. S. Boehm, S. Y. Kim, S. E. Moody, I. F. Dunn, A. C. Schinzel, P. Sandy, E. Meylan, C. Scholl, S. Frohling, E. M. Chan, M. L. Sos, K. Michel, C. Mermel, S. J. Silver, B. A. Weir, J. H. Reiling, Q. Sheng, P. B. Gupta, R. C. Wadlow, H. Le, S. Hoersch, B. S. Wittner, S. Ramaswamy, D. M. Livingston, D. M. Sabatini, M. Meyerson, R. K. Thomas, E. S. Lander, J. P. Mesirov, D. E. Root, D. G. Gilliland, T. Jacks, W. C. Hahn, Systematic RNA interference reveals that oncogenic KRAS-driven cancers require TBK1. *Nature* **462**, 108–112 (2009).
89. H. L. Wang, T. W. Lai, Optimization of Evans blue quantitation in limited rat tissue samples. *Sci. Rep.* **4**, 6588 (2014).
90. N. Mikolajewicz, E. A. Zimmermann, B. M. Willie, S. V. Komarova, Mechanically stimulated ATP release from murine bone cells is regulated by a balance of injury and repair. *eLife* **7**, e37812 (2018).

Acknowledgments

Funding: This work was supported by the National Natural Science Foundation of China (82002339 to J.G. and 81820108020 to C.Z.), the Shanghai Frontiers Science Center of Degeneration and Regeneration in Skeletal System (BJ1-9000-22-4002), and the Science and Technology Project of Quanzhou City (2020N079s and 2019C069R). **Author contributions:** J.G., M.Z., and C.Z. provided the essential ideas and designed the experiments. D.L., P.L., and H.L. performed research. D.L., P.L., H.L., S.T., B.W., Y.L., Y.G., Y.H., H.Z., L.S., Y.Zo., J.Y., P.C., Z.C., P.D., and Y. Zh. analyzed the data. D.L., P.L., and H.L. drafted the manuscript. J.G., M.Z., C.Z., and J.P. revised the manuscript. **Competing interests:** The authors declare that they have no competing interests. **Data and materials availability:** All data needed to evaluate the conclusions in the paper are present in the paper and/or the Supplementary Materials (https://doi.org/10.6084/m9.figshare.25654188.v1). scRNA-seq and bulk RNA-seq datasets that are originally reported in this paper have been deposited in the Gene Expression Omnibus (GEO) database under the accession code: GSE205671 (Dendra2-enrichment of $Dmp1^{Cre}$-$Cox8^{Dendra2}$ mouse brains sequencing), GSE210187 ($Dmp1^{Cre}$-$Mfn2^{fl/fl}$ and age-matched WT mouse brains sequencing); GSE206414 (bulk RNA-seq of bENd.3 endothelial cells). The sequencing work of 1M ($n = 1$), 6M ($n = 1$), and 20M ($n = 1$) WT male mouse brains performed by our group was reanalyzed here, which has been published and deposited by us previously under the GEO number of GSE169606.

Submitted 14 August 2023
Accepted 24 May 2024
Published 28 June 2024
10.1126/sciadv.adk2913